

1 **Field assessments on impact of CO₂ concentration fluctuations along with complex**
2 **terrain flows on the estimation of the net ecosystem exchange of temperate forests**

3 Dexiong Teng^{1,2}, Jiaojun Zhu^{1,2,3,*}, Tian Gao^{1,2,3}, Fengyuan Yu^{1,2}, Yuan Zhu^{1,2}, Xinhua
4 Zhou^{3,4}, Bai Yang⁴

5 1 CAS Key Laboratory of Forest Ecology and Silviculture, Institute of Applied Ecology, Chinese
6 Academy of Sciences, Shenyang 110000, China

7 2 Qingyuan Forest CERN, National Observation and Research Station, Liaoning Province,
8 Shenyang 110016, China

9 3 CAS-CSI Joint Laboratory of Research and Development for Monitoring Forest Fluxes of Trace
10 Gases and Isotope Elements, Institute of Applied Ecology, Chinese Academy of Sciences,
11 Shenyang 110016, China

12 4 Campbell Scientific Incorporation, Logan, Utah 84321, USA

13 *** Corresponding Author: Jiaojun Zhu**

14 Tel : +86 24 83970342

15 Email: jiaojunzhu@iae.ac.cn

16 **Abstract**

17 The CO₂ storage (F_s) is the cumulation or depletion in CO₂ amount over a period
18 in an ecosystem. Along with the eddy-covariance flux and wind-stream advection of
19 CO₂, it is a major term in the net ecosystem CO₂ exchange (NEE) equation and even
20 dominates in the equation under a stable atmospheric stratification while this equation
21 is used for forest ecosystems over complex terrains. However, estimating the F_s remains
22 challenging due to the frequent gusts and random fluctuations in boundary-layer flows
23 that arouse tremendous difficulties in catching the true trend of CO₂ changes for its
24 storage estimation from eddy-covariance along with the atmospheric profile techniques.
25 Using the measurements from Qingyuan Ker Towers equipped with NEE instrument
26 systems separately covering mixed-broadleaf, oak, and larch forests towers in a
27 mountain watershed, this study investigates the gust periods and CO₂ fluctuation
28 magnitudes while examining their impact on F_s estimation in relation to the terrain
29 complexity index (TCI). The gusts induce CO₂ fluctuations at numerous periods of 1 to
30 10 min over two hours. Diurnal, seasonal, and spatial differences ($P < 0.01$) in the
31 maximum amplitude of CO₂ fluctuations (A_m) ranges from 1.6 to 136.7 ppm and these
32 difference in a period (P_m) at the same significant level ranges 140 to 170 second. The
33 A_m and P_m are significantly correlated to the magnitude and random error of F_s with
34 diurnal and seasonal differences. These correlations decrease as CO₂ averaging time
35 windows becomes longer. To minimize the uncertainties of F_s , a constant [CO₂]
36 averaging time window for the F_s estimates is not ideal. Dynamic averaging time
37 windows and a decision-level fusion model can reduce the potential underestimation of

38 F_s by 29%–33% for temperate forests in complex terrains. The relative contribution of
 39 F_s to the 30-min NEE observations ranged from 17% to 82% depending on turbulent
 40 mixing and TCI. The study’s approach is notable as it incorporates TCI and utilizes
 41 three flux towers for replication, making the findings relevant to similar regions with a
 42 single tower.

43 **Keywords:** Eddy covariance, complex terrain, carbon flux, storage term, carbon
 44 dioxide concentration, random uncertainty

45 **1 Introduction**

46 The accurate estimation of the net ecosystem exchange (NEE) of carbon dioxide
 47 (CO_2) in forest ecosystems is crucial for a comprehensive understanding of the global
 48 carbon cycle. The eddy covariance (EC) technique has been widely used in forest
 49 ecosystems due to its capacity to directly measure the NEE while measurement
 50 conditions satisfy the underlying theory. The EC technique is based on a simplified
 51 mass conservation equation (after the Reynolds averaging), given by:

$$\begin{aligned}
 \text{NEE} = & \underbrace{\frac{1}{V_m} \int_0^h \left(\frac{\partial \bar{c}}{\partial t} \right) dz}_{\text{I}} + \underbrace{\frac{1}{V_m} (\overline{w'c'})}_h}_{\text{II}} \\
 & + \underbrace{\frac{1}{V_m} \int_0^h \left(\bar{w}(z) \frac{\partial \bar{c}}{\partial z} \right) dz}_{\text{III a}} + \underbrace{\bar{c}(z) \frac{\partial \bar{w}}{\partial z}}_{\text{III b}} dz, \quad (1) \\
 & + \underbrace{\frac{1}{V_m} \int_0^h \left(\bar{u}(z) \frac{\partial \bar{c}}{\partial x} + \bar{v}(z) \frac{\partial \bar{c}}{\partial y} \right) dz}_{\text{IV}}
 \end{aligned}$$

53 where V_m is the volume of dry air in the control volume; c is the CO_2 mixing ratio; t is
 54 the time; h is the measure height; u , v , and w denote the velocity components in the x ,

55 y , and z directions, respectively; and an overbar denotes Reynolds averaging. This
56 equation conceptualizes the NEE within a control volume from the ground to the
57 measurement height (h), while ignoring the horizontal turbulence term divergence
58 (Feigenwinter et al., 2004). In this equation, term I is the CO₂ storage (F_s) representing
59 the change in the average CO₂ concentration (hereafter [CO₂]). Terms II, IIIa, IIIb, and
60 IV represent the vertical turbulent flux (F_c), the vertical advection, the interface vertical
61 mass advection, such as the evaporation process (Webb et al., 1980), and the horizontal
62 advection, respectively.

63 Most flux measurements typically lack the solutions for terms III and IV, and can
64 only estimate the NEE by summing F_c and F_s , and even a significant number of sites
65 ignored the F_s . The F_s in the vertical gas column within a canopy can be substantial,
66 requiring attention in NEE estimates (Aubinet et al., 2000). The F_s contributes ~60% to
67 nocturnal turbulent flux underestimation in forest ecosystems with “ideal” topography
68 (Mchugh et al., 2017). Especially, during atmospherically stable periods such as the
69 early morning, sunset, and nighttime transitions, the F_s has a significant impact on the
70 NEE. For 30-min ecosystem carbon flux measurements, ignoring F_s would
71 underestimate the NEE (Zhang et al., 2010). The F_s value typically ranges from -2 to
72 $-5 \mu\text{mol m}^{-2} \text{s}^{-1}$ in the early morning, and the F_s is about $1-3 \mu\text{mol m}^{-2} \text{s}^{-1}$ after sunset
73 for temperate forests. The effect of the F_s on the NEE of forest ecosystems decreases
74 with the increase of timescale (Li et al., 2020). However, neglecting the F_s value can
75 lead to a misunderstanding of the CO₂ exchange processes, such as ecosystem
76 respiration and photosynthesis, and their relationship with key control factors such as

77 solar radiation, temperature, and moisture (Mchugh et al., 2017). Therefore, it is
78 imperative not to overlook F_s to ensure more precise NEE estimates of forest
79 ecosystems, particularly in complex terrains.

80 Despite the challenges inherent in monitoring forest conditions, understanding the
81 carbon flux of forest ecosystems in complex terrains or with heterogeneous underlying
82 surfaces remains an area of great interest. Topography complexity plays a complex role
83 in the transportation of momentum, energy, and mass in the atmospheric boundary layer,
84 with direct impacts on the airflow patterns, spatiotemporal characteristics, and gas
85 concentration fluctuations (Sha et al., 2021; Finnigan et al., 2020). Differences in
86 airflow along the slope, lateral CO_2 discharge downhill, and spatiotemporal variations
87 in soil respiration result in the CO_2 outflow from slopes and valleys lagging behind the
88 flat top of the mountain (De Araújo et al., 2010). At night, under stable atmospheric
89 stratification, cold air moves from valley forest canopy to the ground the and then flows
90 to low-lying areas, causing a “carbon pooling” effect. The gradient of $[\text{CO}_2]$ below the
91 EC sensors fluctuates significantly, and the cold air discharge above the canopy reduces
92 CO_2 storage, leading to an underestimation of forest ecosystem respiration (Yao et al.,
93 2011; De Araújo et al., 2008; De Araújo et al., 2010).

94 According to the theoretical definition, F_s estimates are derived by averaging the
95 $[\text{CO}_2]$ of the control volume at the beginning and the end of the EC averaging period
96 (30 min or 1 h) and dividing by the EC averaging period (Finnigan, 2006). The
97 estimation of F_s at numerous sites frequently employs a vertical profile system. This
98 approach operates under the assumption that the F_s represents the integration of the time

99 derivative of the vertically determined column-averaged [CO₂]. It is noteworthy that
100 the column-averaged [CO₂] may not accurately represent the average [CO₂] of the
101 control volume in cases of inadequate air mixing, leading to insufficient sampling.
102 Previous study showed that relying solely on tower-top measurements can lead to
103 underestimation of F_s by up to 34% compared to the eight-level profile approach (Gu
104 et al., 2012). The NEE magnitude with the F_s based on the 2-min [CO₂] averaging time
105 window (instantaneous concentration approach) was found to be 5% higher than that of
106 the 30-min-window-based F_s (averaging concentration approach), particularly during
107 nighttime in the growing season (Wang et al., 2016). A proper measuring system with
108 improving the horizontal representativeness can reduce the bias of F_s to 2–10%
109 (Nicolini et al., 2018). Most research has examined how vertical and horizontal gas
110 concentration sampling point distribution affects the uncertainty in F_s estimation
111 (Bjorkegren et al., 2015; Wang et al., 2016; Yang et al., 2007; Yang et al., 1999), with a
112 small number of studies examining the effect of [CO₂] sampling frequency on the F_s
113 (Finnigan, 2006; Heinesch et al., 2007). Certain studies have experimentally validated
114 new concepts, such as correlating the gas sampling point concentration with the
115 horizontal distribution (Nicolini et al., 2018). Some studies have approached the true
116 value theoretically, such as through defining the control volume represented by flux
117 measurements (Metzger, 2018; Xu et al., 2019). However, the number of complete
118 column samples required to describe the column-averaged [CO₂] of each 30-min or 1-
119 h F_s estimate is still undetermined.

120 Previous studies have emphasized the significance of the F_s to the NEE and the

121 influence of [CO₂] dynamics on F_s estimates in complex terrains. To overcome any
122 disparities between sensors and obtain precise changes in the [CO₂] gradient above and
123 below the forest canopy, individual gas analyzers are extensively utilized to measure
124 [CO₂] levels vertically (Siebicke et al., 2011). However, a single gas analyzer introduces
125 time delays when monitoring multi-point [CO₂] curves. Accurately determining the F_s
126 estimates can be challenging due to the spatial and temporal resolution of [CO₂]
127 measurements (Wang et al., 2016). The random error of the F_s estimates using one
128 complete column sample is considerably high due to short-term [CO₂] fluctuations
129 (Nicolini et al., 2018). The calculation of the F_s using time-averaged [CO₂] profiling
130 leads to significant information loss at high frequency, resulting in a substantial
131 underestimation bias. Furthermore, time-averaged [CO₂] profiling is employed to
132 represent the [CO₂] average within control volume due to resource constraints. This
133 leads to the gap that the systematic bias and random error in F_s estimate are
134 irreconcilable. This issue necessitates further efforts to characterize [CO₂] fluctuations
135 across different sites and demonstrate the mechanisms influencing F_s magnitudes,
136 uncertainties, and their contributions to NEE observations in complex terrains. Thus,
137 this study aims to bridge this gap by introducing a statistical method to estimate F_s
138 values and their uncertainties.

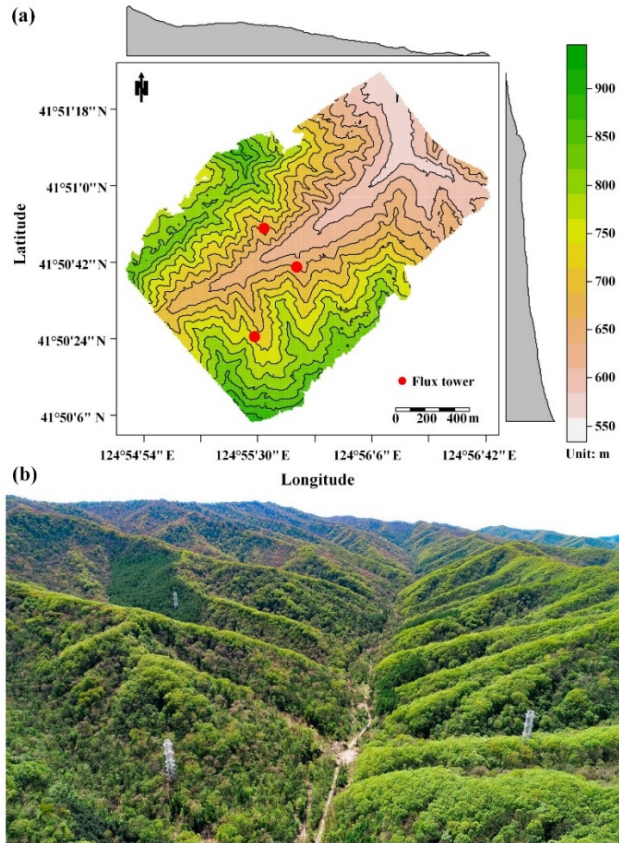
139 This paper employed an innovative EC experimental setup with three flux towers
140 (Qingyuan-Ker Towers) to monitor three typical types of temperate forest stands
141 located in complex terrains in northeastern China. This study introduces a decision-
142 level fusion model based on weighing the underestimation bias and random error of the

143 F_s to obtain more accurate results. The objectives of this study were to: 1) compare
144 diurnal, seasonal, and spatial differences in $[CO_2]$ fluctuations, F_s , and its uncertainty;
145 2) examine the variation in F_s uncertainty with different $[CO_2]$ averaging time windows;
146 and 3) investigate the response of F_s and its uncertainty to $[CO_2]$ fluctuations, wind
147 above the canopy, and terrain complexity, and quantify the impact of the F_s on the NEE
148 estimates under these conditions.

149 **2 Materials and methods**

150 2.1 Study site and instrumental set-up

151 This study was conducted in temperate forests in a watershed based on the Ker
152 towers (Zhu et al., 2021; Gao et al., 2020), situated in northeast China ($41^{\circ}50'N$,
153 $124^{\circ}56'E$). The region experiences a temperate continental monsoon climate, with an
154 average annual temperature of $4.3^{\circ}C$ and annual rainfall of 758 mm from 2010 to 2021
155 (Li et al., 2023). The Ker towers consist of three 50-m-high EC towers (Fig. 1) that
156 observe a mixed broadleaved forest (MBF), a Mongolian oak forest (MOF), and a Larch
157 plantation forest (LPF).



158

159 Fig. 1 Overview of the study area. The first map (a) depicts the topography of the study site, with
 160 black curves indicating elevation contours, and marginal distributions represented as a gray graph,
 161 averaged over rows and columns. The second image (b) features an aerial photograph of the
 162 Qingyuan-Ker towers captured in the growing season (Gao et al., 2020).

163 The basic information regarding Ker towers in this study is presented in Table 1.
 164 The CPEC310 integrated system from Campbell Scientific comprising an EC155
 165 closed-path infrared gas analyzer (IRGA) and a CSAT3A sonic anemometer, was
 166 employed to monitor the three-dimensional wind speed and CO₂/H₂O concentrations
 167 (10 Hz). The atmospheric profiling system (AP200, Campbell Scientific Ltd., Logan,
 168 UT, USA) was utilized to measure the CO₂/H₂O concentrations with eight height levels.
 169 Each level was measured for 15 s (with 10 s for the flushing of the manifold and 5 s for
 170 logging the average), leading to a measurement cycle of 2 min. Due to calibration, filter
 171 changes, and rugged weather, 10% CPEC data and 3% AP200 data were missed in our

172 study period.

173 Table 1 Basic information of Ker towers

Forest	Mixed broad-leaved	Mongolian oak	Larch plantation
Experiment period	Jan 01, 2020– Dec 31, 2021	Jan 01, 2020– Dec 31, 2021	Jan 01, 2020– Dec 31, 2021
Elevation (m)	634	669	721
Slope (°)	14.8 ± 2.1	19.1 ± 2.9	16.2 ± 5.3
Canopy height (m)	21.5 ± 1.8	13.9 ± 0.6	19.5 ± 0.6
Leaf area indices	3.0 ± 0.5	3.1 ± 0.8	3.9 ± 0.6
Eddy covariance system	CPEC310	CPEC310	CPEC310
Eddy covariance sensor height (m)	46	46	36
Atmospheric profiling system	AP200	AP200	AP200
Profile heights (m)	0.5, 2, 6, 11, 16, 21, 26, 36	0.5, 2, 6, 11, 16, 21, 26, 36	0.5, 2, 6, 11, 16, 21, 26, 36

174 2.2 Calculation of storage flux

175 Averaging the [CO₂] in a time window was utilized to calculate the F_s values, in
176 addition to data on the air pressure, CO₂/H₂O molar fractions, and air temperature at
177 different heights above the ground surface (Finnigan, 2006; Montagnani et al., 2018;
178 Xu et al., 2019). The molar mixing ratio and mass mixing ratio are conserved quantities
179 with the variation of air temperature, air pressure, and water vapor concentration,
180 whereas the molar fraction is not. This study determined the F_s using the molar mixing
181 ratio obtained from CO₂/H₂O molar fraction observations, applying the ideal gas law
182 and Dalton's partial pressure law (Montagnani et al., 2009). The water vapor molar
183 mixing ratio (χ_v) in mmol mol⁻¹ is given by

$$\chi_v = \frac{c_v}{1 - c_v \times 10^{-3}}, \quad (2)$$

184 where c_v is the water vapor molar fraction in mmol mol^{-1} , and the CO_2 molar mixing

185 ratio (χ_c) in $\mu\text{mol mol}^{-1}$ is given by

$$\chi_c = \frac{c_c}{1 - c_v \times 10^{-3}}, \quad (3)$$

186 where c_c is the CO_2 molar fraction in $\mu\text{mol mol}^{-1}$.

187 The dry air density ($\bar{\rho}_d$) in mol m^{-3} is calculated as follows:

$$\bar{\rho}_d = \frac{\bar{P}}{(\bar{T} + 273.15) \times (R^* + \chi_v \times 10^{-3} \cdot R^* \cdot M_d/M_v)}, \quad (4)$$

188 where R^* is the air gas constant ($8.31441 \text{ Pa m}^3 \text{ K}^{-1} \text{ mol}^{-1}$), \bar{P} is the air pressure in

189 Pa, and \bar{T} is the average air temperature in Celsius. M_d and M_v are the dry air and

190 water vapor molar mass ($18.015 \text{ g mol}^{-1}$), respectively. M_d is calculated from the CO_2

191 molar mixing ratio (Khélifa et al., 2007):

$$M_d = 28.9635 + M_c \cdot (\chi_c \times 10^{-6} - 0.0004), \quad (5)$$

192 where M_c is the carbon molar mass ($12.011 \text{ g mol}^{-1}$).

193 The F_s estimated from eight-level profiles are calculated as follows:

$$F_s = \bar{\rho}_d \int_0^h \frac{d\bar{\chi}_c}{dt} dz \doteq \bar{\rho}_d \sum_{i=1}^8 \frac{\Delta\bar{\chi}_{c_i} \Delta h_i}{\Delta t}, \quad (6)$$

194 where $\bar{\chi}_c$ is the average CO_2 molar mixing ratio and Δh_i is the height represented by

195 each level.

196 When measuring the F_s by sampling CO_2 at several levels using a single analyzer,

197 the synchronous observations of CO_2 profile are impractical. Consequently, discrete

198 temporal sampling and time averaging become necessary. To ensure the temporal

199 alignment of F_s with F_c , the average $[\text{CO}_2]$ measurements within the control volume at

200 the beginning and end (t) of an averaging period (30 min) are calculated by averaging

201 over a time window (τ min) as follows:

$$\bar{\chi}_{c_i} = \frac{2}{\tau} \sum_{t-\frac{\tau}{2} < t \leq t+\frac{\tau}{2}} \chi_{c_i}(t), \quad (7)$$

202 where $\tau = 4, 8, \dots, 28$ min. Theoretically, the time window should be kept as short as
203 possible in comparison to the turbulence flux averaging period to comply with the
204 principle of Reynolds decomposition. We use large windows here for CO₂ averaging in
205 an attempt to demonstrate the effects of different window sizes on the accuracy of
206 storage flux estimates.

207 2.3 Data analysis

208 To evaluate the impact of [CO₂] fluctuations on F_s measurements and its
209 corresponding uncertainty, empirical modal decomposition (EMD) and Fourier
210 spectrum analysis (FSA) were used to extract the period and amplitude of fluctuations
211 in the high-frequency [CO₂] time series (10 Hz). EMD was used to decompose the [CO₂]
212 time series into intrinsic mode functions based on local signal properties (Huang and
213 Wu, 2008), which yield instantaneous frequencies as functions of time, allowing for the
214 identification of embedded structures of eddies. EMD is applicable to non-linear and
215 non-stationary processes (Huang et al., 1998). The period and amplitude of [CO₂]
216 fluctuations above the forest canopies reflected the eddy size. Subsequently, the
217 maximum period and amplitude of [CO₂] fluctuations in a short term (2h) was
218 indicative of large eddies under the influence of gust.

219 Due to the diurnal and seasonal variability of flux measurements, this study
220 defined the transition period and growing season. The solar elevation angle was used

221 to define the transition period as 1-h before sunrise (sunset) to 2-h after sunrise (sunset).
222 The growing degree days (GDDs) were calculated using the base temperature (T_{base}) to
223 determine the beginning and end of the growing season, and the formula was as follows
224 (Mcmaster and Wilhelm, 1997):

$$GDD = \frac{1}{2}(T_{max} + T_{min}) - T_{base}, \quad (8)$$

225 where T_{base} is 6°C. Considering the persistent demand of temperature to support
226 vegetation growth, the fourth day of the first GDD greater than zero (less than zero)
227 over a span of five consecutive days was defined as the starting (ending) time of the
228 growing season.

229 The main data processing and analysis steps are outlined below:

230 1. EMD and Fourier spectrum analysis of $[CO_2]$ high-frequency time series were
231 used to extract the maximum amplitude (A_m) and corresponding period (P_m) of $[CO_2]$
232 fluctuations every 2 h. The data were divided into two subsets based on P_m , with a cut-
233 off of 150 s.

234 2. CO_2 storage fluxes were calculated for different $[CO_2]$ averaging time windows
235 (τ), ranging from 4 to 28 min in increments of 4 min.

236 3. The standardized major axis (SMA) regression model (Warton et al., 2012) was
237 used to compare the slope differences (bias) between F_{s_τ} and $F_{s_{28}}$ for different P_m and
238 the forest stands. The SMA model offers routines for comparing parameters a and b
239 among groups for symmetric problems.

240 4. The normalized root mean square error (NRMSE) and slope were used to
241 evaluate the relative error and bias between F_{s_τ} and $F_{s_{28}}$. The NRMSE is calculated as

242 follows:

$$NRMSE = 100 \times \sqrt{\frac{\sum_{i=1}^N (F_{s_\tau}^{(i)} - F_{s_{28}}^{(i)})^2}{\sum_{i=1}^N (F_{s_{28}}^{(i)} - \overline{F_{s_{28}}})^2}} \quad (9)$$

243 where i indicates the i^{th} observation.

244 5. The normalized weighting coefficient (w) of F_{s_τ} was estimated based on the
245 NRMSE and slope (Wang et al., 2020). The details are shown in Appendix A1. Then,
246 using the decision-level fusion model, F_{s_comb} was calculated as follows:

$$F_{s_comb} = w_1^* \cdot F_{s_4} + w_2^* \cdot F_{s_8} + \dots + w_7^* \cdot F_{s_{28}} \quad (10)$$

247 The decision-level fusion model automatically assigned weights to the F_s based on
248 different $[\text{CO}_2]$ averaging time windows. Its purpose in this study was to balance the
249 relative error and bias of F_s estimates caused by $[\text{CO}_2]$ sampling. The analysis was
250 performed using the EMD and smatr R packages (Warton et al., 2012; Huang et al.,
251 1998).

252 2.4 Uncertainty analysis

253 To improve the accuracy of estimating the uncertainty of F_s using individual tower,
254 this work has made modifications to the 24-h difference method by extending the
255 sampling time windows and applying meteorological condition constraints (Hollinger
256 and Richardson, 2005). This method trades time for space to estimate the uncertainty
257 of F_s . To determine the uncertainty of F_s , expressed as $\sigma(\varepsilon_s)$, in this case, we compared
258 the observations at moment i within a day to the average of several observations during
259 a similar period and with similar meteorological conditions. The specific computations
260 were as follows:

$$\bar{F}_s^{(i)} = \frac{1}{N} \sum_{t \in \Omega, \lambda_t \in \Lambda} I(\lambda_t) \cdot F_s^{(t)}, \quad (11)$$

$$\Lambda = \{\lambda_t | \sqrt{\frac{(u_*^{(\lambda_t)} - u_*^{(i)})^2}{\sigma_{u_*}} + \frac{(\text{Ta}(\lambda_t) - \text{Ta}^{(i)})^2}{\sigma_{\text{Ta}}} + \frac{(\text{H}(\lambda_t) - \text{H}^{(i)})^2}{\sigma_{\text{H}}}} < \delta\}, \quad (12)$$

$$\varepsilon_s^{(i)} = F_s^{(i)} - \bar{F}_s^{(i)}, \quad (13)$$

$$\bar{\varepsilon}_s^{(i)} = \frac{1}{N} \sum_{t \in \Omega, \lambda_t \in \Lambda} I(\lambda_t) \cdot \varepsilon_s^{(t)}, \quad (14)$$

$$\sigma(\varepsilon_s)^{(i)} = \sqrt{\frac{1}{N} \sum_{t \in \Omega, \lambda_t \in \Lambda} I(\lambda_t) \cdot (\varepsilon_s^{(t)} - \bar{\varepsilon}_s^{(i)})^2}, \quad (15)$$

261 where Ω was the moment interval ($i-0.5$ h, $i+0.5$ h) within a certain time window (15
 262 d); I was indicator function; the set Λ represented consisted of elements that meet
 263 similar meteorological conditions, including the u_* , air temperature (Ta), and sensible
 264 heat flux (H); σ_{u_*} , σ_{Ta} , and σ_{H} are the standard deviation of the u_* , Ta, and H,
 265 respectively; δ was the threshold of Euclidean distance; and ε_s was the random error
 266 of F_s .

267 After estimating the uncertainty of F_s , this study extended the work conducted by
 268 Richardson et al. (2008) to analyze its relationship with the magnitude of flux
 269 measurements ($|F_s|$), $[\text{CO}_2]$ fluctuations (A_m and P_m), u_* , and terrain complexity index
 270 (TCI). A comprehensible description of the TCI can be found in Appendix A2. This
 271 relationship can be approximated by using the following equation:

$$\sigma(\varepsilon_s) = \beta_0 + \sum_{i=1} \beta_i \cdot x_i, \quad (16)$$

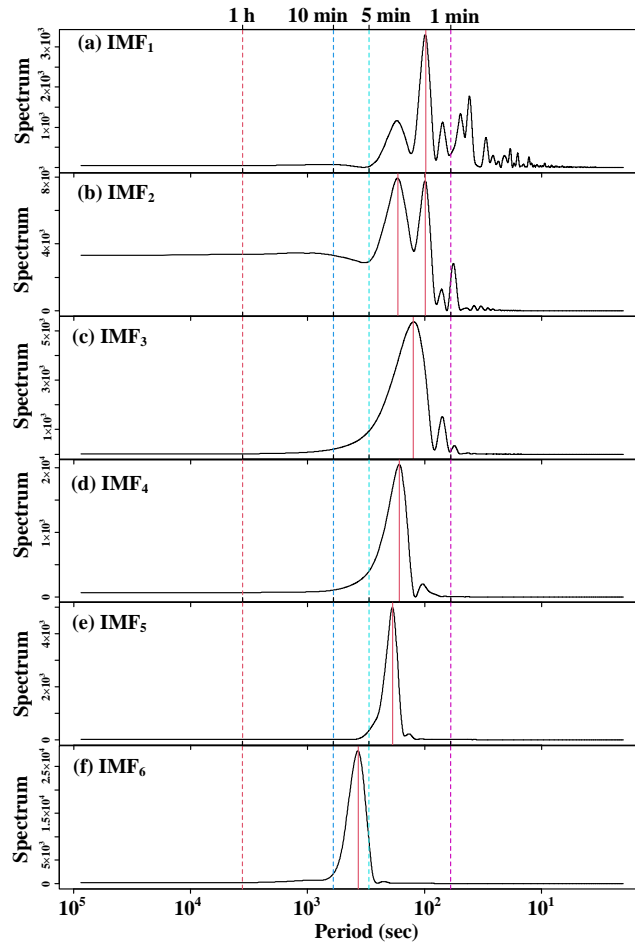
272 where the nonzero intercept term β_0 indicates the size of the random uncertainty as
 273 x_i approaches 0, which varies with the observation site, with larger value of β_0

274 indicating greater uncertainty. The slope term β_i indicates the sensitivity of the size of
275 the random uncertainty of x_i , with smaller β_i values indicating a probability
276 distribution of uncertainty closer to white noise.

277 **3 Results**

278 3.1 Characterization of [CO₂] fluctuation and F_s variations

279 The [CO₂] high-frequency time series above the forest canopies were decomposed
280 using EMD, followed by spectral analysis to extract the fluctuation period and
281 amplitude of [CO₂] at different time scales. As depicted in Fig. 2, it became evident that
282 the [CO₂] above the canopies displayed short-term fluctuations with periods ranging
283 from 1 to 10 min, and the amplitude of these fluctuations showed an increasing trend
284 with longer periods. This observation strongly suggested the presence of large eddies
285 influenced by gusts above the canopies, and these eddies were responsible for the
286 increasing amplitude of [CO₂] fluctuations as their size increased.



287

288 Fig. 2 Power spectral density of the intrinsic mode function (IMF) of above-canopy CO₂
 289 concentrations in the Mongolian oak forest on July 2, 2020 (24 h).

290 To examine the spatio-temporal variations in large eddies, this study compared the
 291 A_m and P_m values above canopies across different forest stands. The analysis utilized
 292 data from daytime, nighttime, and transition periods in both the growing and dormant
 293 seasons. The averages of A_m and P_m averages for the above-canopy [CO₂] in the three
 294 forest stands ranged from 1.588 to 136.667 ppm and from 2.313 to 2.784 min,
 295 respectively (Table 2). Fig. 3 demonstrated significant seasonal and diurnal differences
 296 ($P < 0.01$) in P_m , with higher values during daytime in the growing season, and lower
 297 values during the daytime in the dormant season. Moreover, P_m was significantly
 298 different ($P < 0.01$) among different forest stands during the same time period, with

299 MBF stand having the highest values, followed by the MOF, and the lowest values in
 300 the LPF. During the growing season, the A_m values were significantly higher than those
 301 during the dormant season, with both daytime and nighttime values also exhibiting
 302 significant differences ($P < 0.01$) among different forest stands. This observation
 303 provided evidence of significant spatio-temporal variability in large eddies influenced
 304 by gusts.

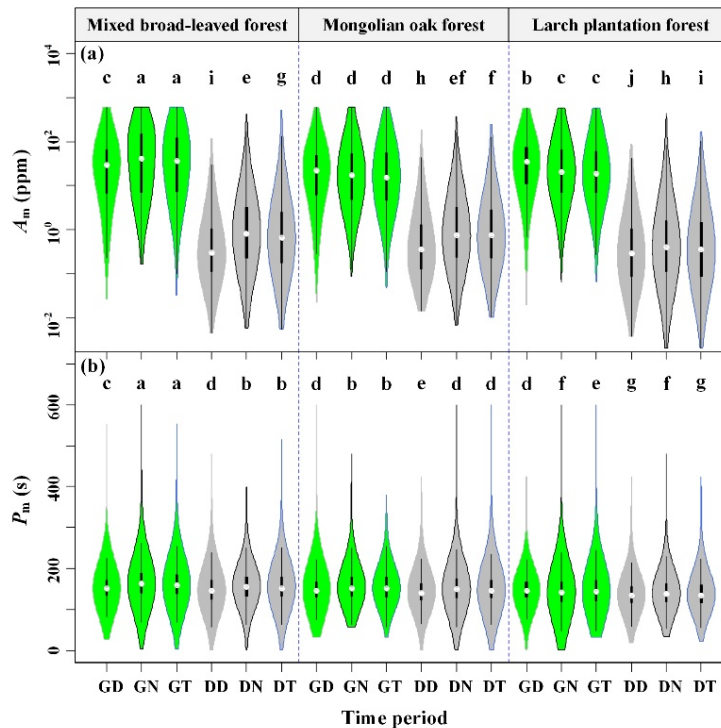
305 Table 2 Mean of the A_m in ppm and P_m in second (s) for three forest stands at different
 306 periods

Variable	Tower site	Growing season			Dormant season		
		DT ¹	NT ²	TP ³	DT	NT	TP
A_m ⁴ (ppm)	MBF ⁶	57.932	139.667	136.717	2.219	5.212	4.944
	MOF ⁷	36.160	57.945	55.777	2.699	5.175	4.637
	LPF ⁸	52.688	58.816	60.147	1.588	2.985	2.456
P_m ⁵ (s)	MBF	154.563	167.024	164.824	158.449	151.428	158.121
	MOF	151.986	160.633	159.146	153.091	147.491	153.274
	LPF	149.003	143.950	145.696	143.458	138.794	142.009

307 ¹ DT represents daytime; ² NT represents nighttime; ³ TP represents transition period. ⁴ A_m
 308 represents the maximum amplitude of short-term CO₂ concentration fluctuations; ⁵ P_m represents
 309 the corresponding period of maximum amplitude. ⁶ MBF represents mixed broad-leaved forest; ⁷
 310 MOF represents Mongolian oak forest; ⁸ LPF represents Larch plantation forest.

311 To estimate the uncertainty of F_s using an individual tower, a comprehensive
 312 analysis of its diurnal and seasonal dynamics, as well as the functional relationship
 313 between F_s and u^* , was necessary. Significant diurnal variations and seasonal
 314 differences in F_s were observed across the three forest stands, as shown in Fig. 4. During
 315 the growing season, the median diurnal variation of F_s for the three forest stands ranged
 316 from -2.960 to $2.647 \mu\text{mol m}^{-2} \text{s}^{-1}$, whereas during the dormant season, it ranged from

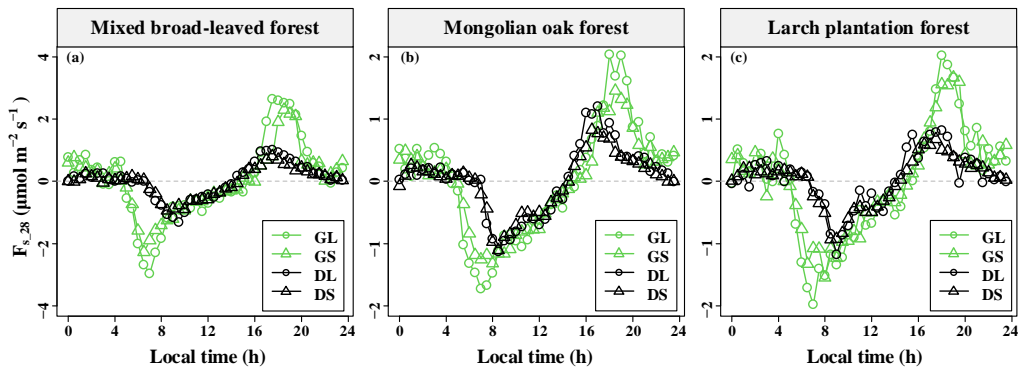
317 -1.306 to $1.012 \mu\text{mol m}^{-2} \text{s}^{-1}$. Comparing the extent of F_s diurnal variation among the
 318 three forest stands, MBF exhibited the largest extent during the growing season, while
 319 the extent of the three forest stands were similar during the dormant season. Notably, it
 320 was observed that the amplitudes for longer P_m values were greater than those for
 321 shorter P_m values. This observation indicated that the larger the eddies, the greater the
 322 magnitude of F_s .



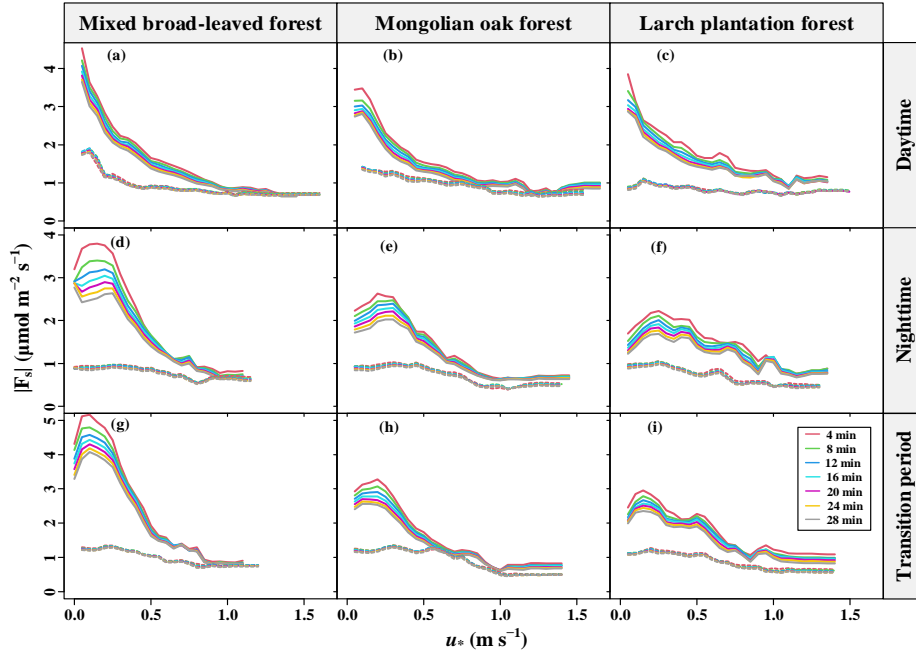
323
 324 Fig. 3 Maximum amplitude (A_m) (a) and corresponding period (P_m) (b) of short-term CO_2
 325 concentration fluctuations in different forest stands for seasonal and diurnal variations, where GD,
 326 GN, GT, DD, DN, and DT denote the growing season daytime, growing season nighttime,
 327 growing season transition period, dormant season daytime, dormant season nighttime, and
 328 dormant season transition period, respectively. Columns with different lowercase letters are
 329 significantly different ($P < 0.05$) according to Fisher's least significant difference test.

330 Furthermore, a u^* threshold value was identified for the variation of F_s with u^*
 331 during daytime in both the dormant and growing seasons (Fig. 5). When u^* fell below
 332 the u^* threshold, the magnitude of F_s ($|F_s|$) decreased with increasing u^* . Conversely,

333 when u^* exceeded the u^* threshold, the $|F_s|$ tended to remain relatively constant. Notably,
 334 a maximum point for the $|F_s|$ was observed when the u^* was less than 0.5 m/s during the
 335 growing season, whereas not during the dormant season. This phenomenon was
 336 particularly evident during the nighttime and transition periods of the growing season,
 337 where $|F_s|$ exhibited an initial increase followed by a subsequent decrease with u^* . These
 338 observations strongly indicated that the effect of the turbulent mixing strength on the
 339 $|F_s|$ over complex terrains was nonlinear and exhibited diurnal and seasonal differences.



340
 341 Fig. 4 Median diurnal variation of CO₂ storage flux (F_s) based on 28-min CO₂ concentration
 342 averaging time windows in the three forest stands during different seasons. GS indicates the
 343 growing season and a short period of maximum amplitude (P_m), GL indicates the growing season
 344 and a long P_m , DS indicates the dormant season and a short P_m , and DL indicates the dormant
 345 season and a long P_m .



346

347 Fig. 5 Magnitudes of CO₂ storage flux ($|F_s|$) determined with different CO₂ concentration average
 348 time windows as a function of the friction velocity (u^*) and moving block averages from all 30-
 349 min data for the years 2020-2021. Dashed and solid lines indicate the dormant and growing
 350 seasons, respectively.

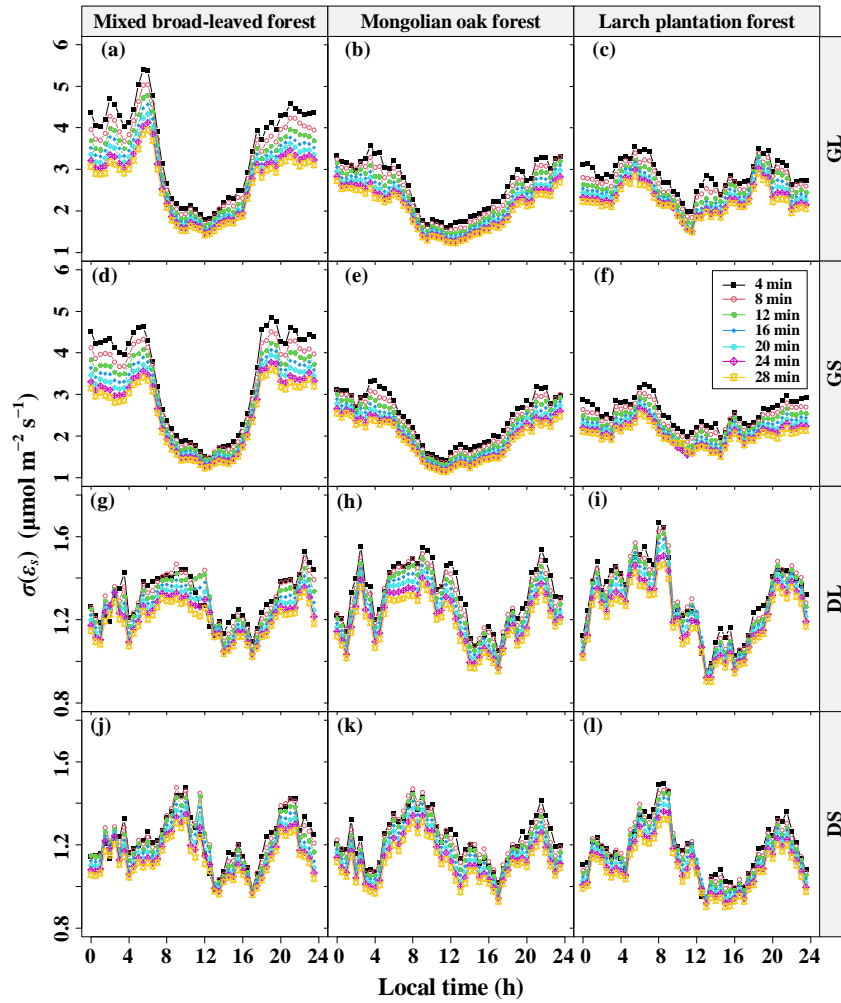
351 3.2 Effect of [CO₂] fluctuations on the F_s and its uncertainty

352 To investigate the influence of the [CO₂] fluctuation periods on the error of F_s
 353 measurement, this study computed the diurnal average of the standard deviation $\sigma(\varepsilon_s)$
 354 of the 30-min F_s uncertainty (ε_s) separately for different P_m values and the seasons. The
 355 overall distribution of ε_s showed a non-normal distribution with a high peak (kurtosis >
 356 2 and $P < 0.05$, results presented in Supplementary Table 1–4). The daily variation
 357 curves of $\sigma(\varepsilon_s)$ at various [CO₂] averaging time windows are presented in Fig. 6. It
 358 was observed that the diurnal variation range of $\sigma(\varepsilon_s)$ was higher during the growing
 359 season compared to the dormant season, regardless of the P_m lengths, indicating a
 360 seasonal difference independent of the P_m . Additionally, during the growing season,
 361 both MBF and MOF demonstrated evident diurnal variation in $\sigma(\varepsilon_s)$, with the peak

362 occurring at night and the trough during the daytime. The diurnal variation range of
363 $\sigma(\varepsilon_s)$ varied across the three forest stands, with MBF exhibiting the largest amplitude.

364 Furthermore, a significantly positive correlation was observed between $\sigma(\varepsilon_s)$ the
365 $|F_s|$ ($P < 0.01$), with site, seasonal, and diurnal differences (Fig. 7). The relationship
366 between $\sigma(\varepsilon_s)$ the $|F_s|$ was characterized by intercepts and slopes ranging from 1.99
367 to $2.82 \mu\text{mol m}^{-2} \text{s}^{-1}$ and from 0.24 to 0.28, respectively (results presented in the
368 Supplementary Tables 5–6). Both decreased as the $[\text{CO}_2]$ averaging time window
369 increased, with the growing season exhibiting larger values compared to the dormant
370 season (results shown in the Supplementary Tables 5–6). These findings suggested that
371 increasing the $[\text{CO}_2]$ averaging time window, results in a reduction of the random error
372 in F_s and the correlation coefficient between $\sigma(\varepsilon_s)$ and $|F_s|$. This indicated a decrease
373 in variability of $\sigma(\varepsilon_s)$ and a behavior similar to white noise.

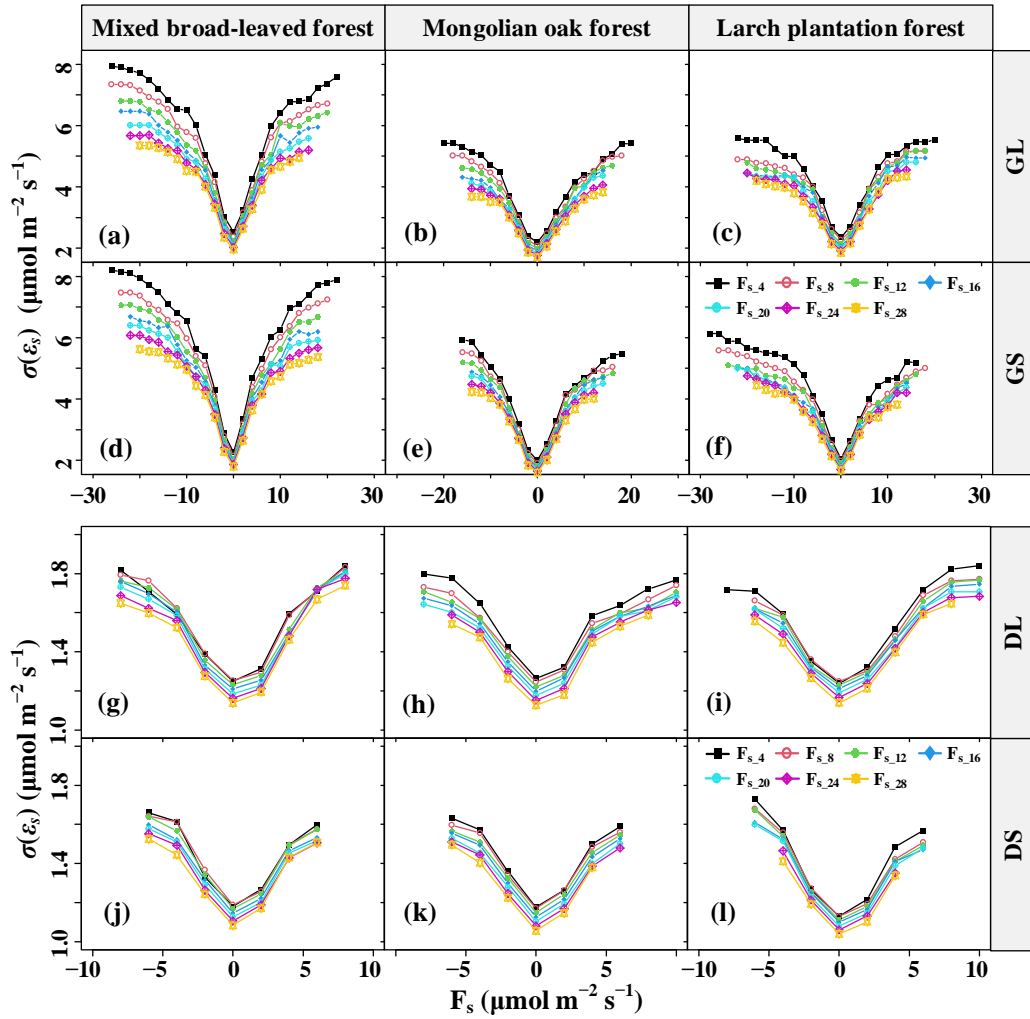
374 To assess the impact of $[\text{CO}_2]$ fluctuations on the error and bias of F_s measurement,
375 this study compared the NRMSE and slopes of F_s based on different $[\text{CO}_2]$ averaging
376 time windows, with reference to the baseline F_{s_28} , across various P_m values, time
377 periods, and sites. As shown in Fig. 8, the NRMSE decreased and approached
378 convergence as the $[\text{CO}_2]$ averaging time windows increased. During both daytime and
379 nighttime in the growing season, the NRMSE corresponding to longer P_m was greater
380 than that corresponding to shorter P_m , while the opposite trend was observed during the
381 dormant season. Additionally, the longer the $[\text{CO}_2]$ averaging time window, the greater
382 the relative underestimation of F_s .



383

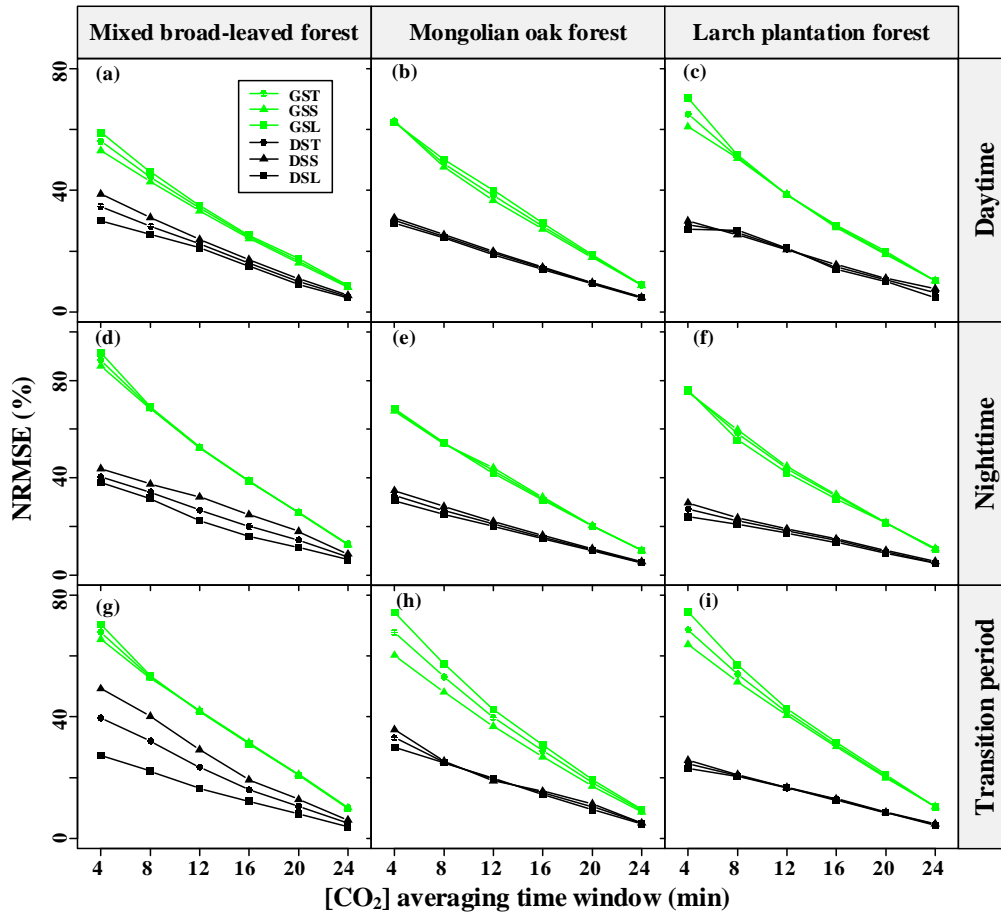
384 Fig. 6 Diurnal variations in the random uncertainty ($\sigma(\varepsilon_s)$) of CO₂ storage flux (F_s) errors (ε_s) at
 385 different CO₂ concentration ($[CO_2]$) averaging time windows and their seasonal differences, where

386 GS indicates the growing season and a short period of maximum amplitude (P_m) of $[CO_2]$
 387 fluctuations, GL indicates the growing season and a long P_m , DS indicates the dormant season and
 388 a short P_m , and DL indicates the dormant season and a long P_m .



389

390 Fig. 7 Random uncertainty $\sigma(\varepsilon_s)$ of CO_2 storage flux (F_s) errors (ε_s) at different CO_2
 391 concentration ($[\text{CO}_2]$) averaging time windows as a function of the F_s magnitude for mixed broad-
 392 leaved forest, Mongolian oak forest, and Larch plantation forest during the growing and dormant
 393 seasons. GS indicates the growing season and a short period of maximum amplitude (P_m) of $[\text{CO}_2]$
 394 fluctuations, GL indicates the growing season and a long P_m , DS indicates the dormant season and
 395 a short P_m , and DL indicates the dormant season and a long P_m .



396

397

398

399

400

401

402

403

Fig. 8 Seasonal and diurnal differences in the normalized root mean square error (NRMSE) of F_s versus the respective $F_{s,28}$ values for different CO_2 concentration ($[CO_2]$) averaging time windows. GST indicates the growing season and does not distinguish the period of maximum amplitude (P_m) of $[CO_2]$ fluctuations, GSS indicates the growing season and a short P_m , GSL indicates the growing season and a long P_m , DST indicates the dormant season and does not distinguish P_m , DSS indicates the dormant season and a short P_m , and DSL indicates the dormant season and a long P_m .

404

405

406

407

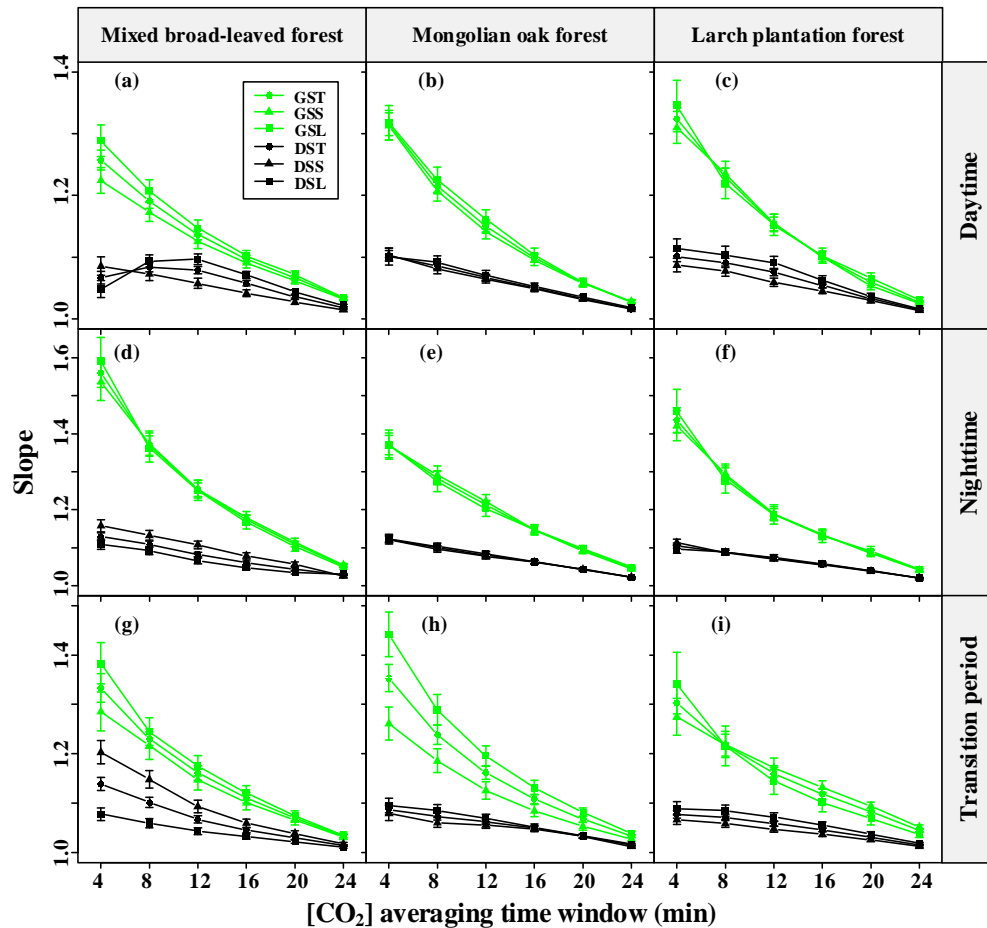
408

409

410

The comparison of slopes between $F_{s,4}$ and $F_{s,28}$ in the three forest stands revealed interesting patterns, as depicted in Fig. 9. During the growing season, the slopes corresponding to the shorter P_m of $[CO_2]$ fluctuations were consistently lower than those for the longer P_m , indicating that the effect of P_m on F_s uncertainty decreased with increasing $[CO_2]$ averaging time windows. However, for the MBF stand (Fig. 9d and Fig. 9g), the slopes corresponding to the shorter P_m of $[CO_2]$ fluctuations during the dormant season nighttime were actually greater than those for the longer P_m , primarily

411 due to diurnal variations in the daily dynamics of F_s . Overall, the influence of P_m on F_s
 412 uncertainty decreased with increasing $[CO_2]$ averaging time windows. This suggested
 413 that averaging $[CO_2]$ reduced the effect of gusts on the random uncertainty in estimating
 414 F_s , but led to a systematic underestimation of F_s .



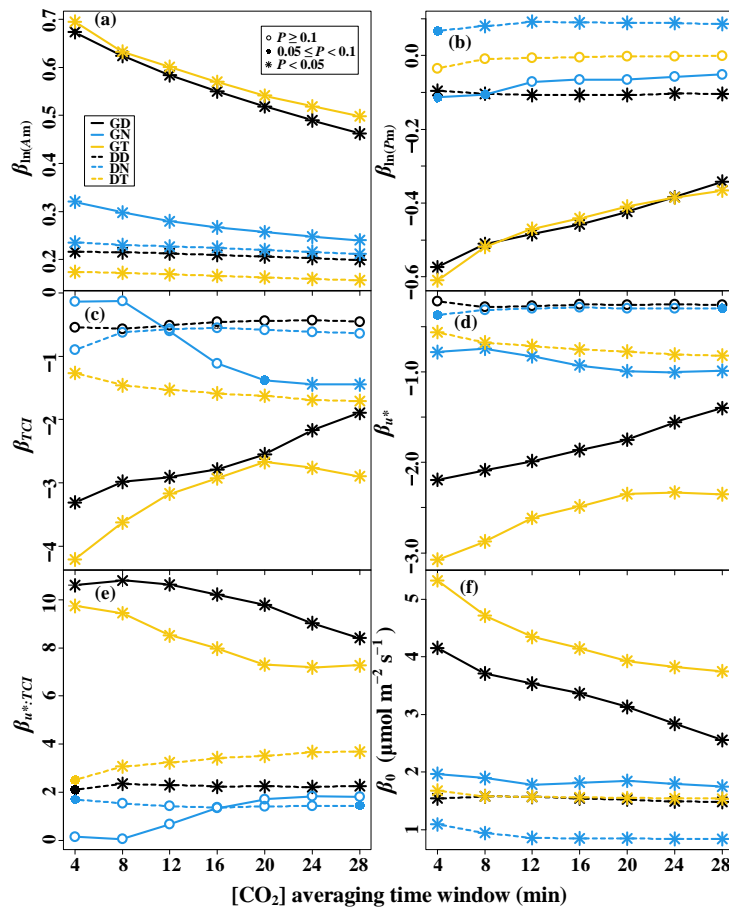
415
 416 Fig. 9 Seasonal and diurnal differences in the slope of CO_2 storage flux (F_s) versus the $F_{s,28}$ for the
 417 different CO_2 concentration ($[CO_2]$) averaging time windows. GST indicates the growing season
 418 and does not distinguish the period of maximum amplitude (P_m) cases, GSS indicates the growing
 419 season and a short P_m , GSL indicates the growing season and a long P_m , DST indicates the
 420 dormant season and does not distinguish P_m , DSS indicates the dormant season and a short P_m ,
 421 and DSL indicates the dormant season and a long P_m .

422 To analyze the effect of $[CO_2]$ fluctuations on $|F_s|$ in complex terrains, this study
 423 developed a multiple linear regression model, considering the interaction effects of
 424 turbulent mixing and terrain complexity on $|F_s|$, as shown in Fig. 10. A_m exhibited a

425 significant positive correlation with $|F_s|$ in all time periods ($P < 0.05$). Conversely, P_m
426 showed a significant negative correlation with $|F_s|$ during the dormant season daytime,
427 the growing season daytime, and the transition periods ($P < 0.05$). Additionally, their
428 correlation coefficient decreased with increasing τ . In Fig. 10d and Fig. 10e, a u^*
429 threshold was observed during the growing season nighttime. When the u^* was below
430 the threshold, higher TCI values resulted in smaller $|F_s|$; whereas when the u^* was above
431 the threshold, higher TCI values led to larger $|F_s|$. During the growing season nighttime
432 and transition periods, u^* showed a significant negative correlation ($P < 0.05$) with $|F_s|$,
433 and the correlation coefficient decreased with increasing TCI values. These
434 observations suggested that the effect of turbulent mixing on the $|F_s|$ uncertainty was
435 regulated by terrain complexity.

436 A multiple linear regression model was used to analyze the effect of $[CO_2]$
437 fluctuations on the random uncertainty of F_s , $\sigma(\varepsilon_s)$, in complex terrains. This model
438 considered the interaction effects of $[CO_2]$ fluctuations and terrain complexity on
439 $\sigma(\varepsilon_s)$, as shown in Fig. 11. As evident from Fig. 11a and Fig. 11e, the A_m exhibited a
440 significant positive correlation ($P < 0.05$) with $\sigma(\varepsilon_s)$ during both the dormant season's
441 nighttime and the growing season. Throughout the transition period of the growing
442 season, P_m displayed a significant negative correlation with $\sigma(\varepsilon_s)$ ($P < 0.05$). The
443 magnitude of these correlation coefficients decreased with the increasing $[CO_2]$
444 averaging time windows. During the transition period of the dormant season, a TCI
445 threshold was observed, with P_m showing a significant positive correlation ($P < 0.05$)
446 with $\sigma(\varepsilon_s)$ when the TCI was below the threshold, and a significantly negative

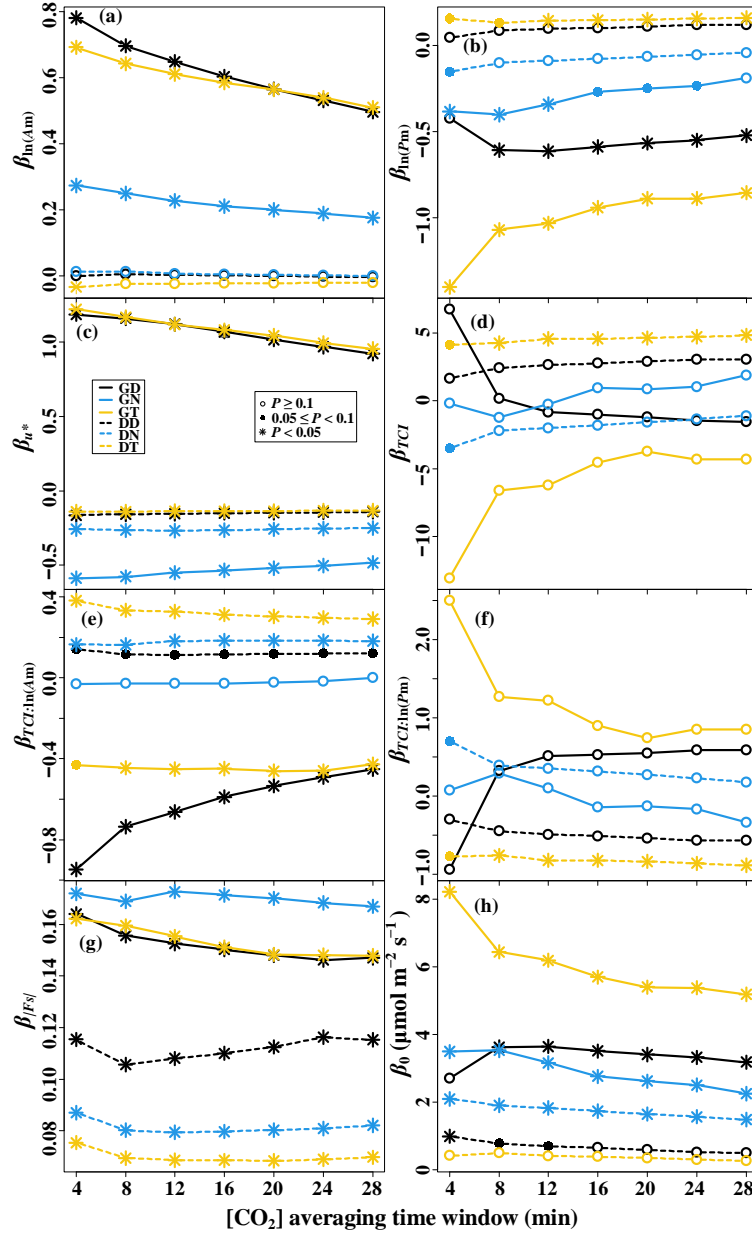
447 correlation ($P < 0.05$) with $\sigma(\varepsilon_s)$ when the TCI exceeded the threshold (Fig. 11b and
 448 Fig. 11f). The u^* showed a significantly negative correlation with $\sigma(\varepsilon_s)$ during the
 449 daytime and transition periods of the growing season ($P < 0.05$), while in other time
 450 periods, u^* was significantly positively correlated with $\sigma(\varepsilon_s)$ ($P < 0.05$). The $|F_s|$
 451 demonstrated a significant positive correlation with $\sigma(\varepsilon_s)$ ($P < 0.05$) in all time
 452 periods, with its correlation coefficient being greater during the growing season than
 453 during the dormant season. These observations suggested that the relationship between
 454 the random uncertainty in F_s and $[\text{CO}_2]$ fluctuations was moderated by topographic
 455 complexity. Increasing the $[\text{CO}_2]$ averaging time window reduced the effect of $[\text{CO}_2]$
 456 fluctuations on the random uncertainty in F_s .



457

458 Fig. 10 Linear regression coefficients of the CO_2 storage flux (F_s) magnitude—driving factors

459 relationships for the seven CO₂ concentration ([CO₂]) averaging time windows. The predictors of of
 460 the multiple linear models are (a) the logarithm of maximum amplitude of [CO₂] fluctuations
 461 (ln(A_m)), (b) the logarithm of the corresponding period of maximum amplitude (ln(P_m)), (c) the
 462 terrain complexity index (TCI), (d) the friction velocity (u*), and (e) the interaction term of TCI
 463 and u*, respectively. (f) β₀ represents the intercept term.



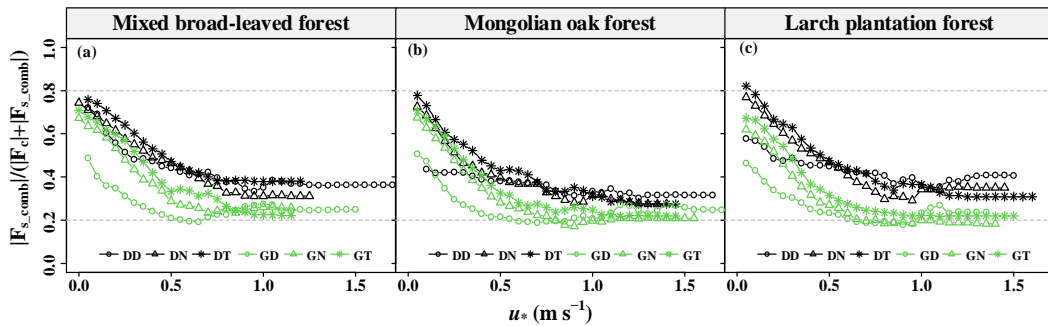
464

465 Fig. 11 Linear regression coefficients of the random uncertainty of CO₂ storage flux ($\sigma(\varepsilon_s)$)—
 466 driving factors relationships determined with Eq. (11) for the seven CO₂ concentration ([CO₂])
 467 averaging time windows. The predictors of the multiple linear models are (a) the logarithm of
 468 maximum amplitude of [CO₂] fluctuations (ln(A_m)), (b) the logarithm of the corresponding period
 469 of maximum amplitude (ln(P_m)), (c) the terrain complexity index (TCI), (d) the friction velocity

470 (u^*), (e) the interaction term of TCI and $\ln(A_m)$, (f) the interaction term of TCI and $\ln(P_m)$, and the
 471 magnitude of storage flux ($|F_s|$), respectively. (h) The intercept term is represented by β_0 .

472 3.3 Effect of CO₂ storage fluxes uncertainty on NEE observations

473 The 30-min F_{s_comb} was obtained by weighing the bias and random error of F_s using
 474 different [CO₂] averaging time windows and P_m values. This study then focused on the
 475 magnitude of F_{s_comb} in relation to the F_c magnitude and its diurnal, seasonal, and site
 476 variations. To assess the significance of F_s in NEE observations, the relative
 477 contribution ratio of F_{s_comb} magnitude ($|F_{s_comb}|/(|F_c|+|F_{s_comb}|)$) was employed. The
 478 $|F_{s_comb}|/(|F_c|+|F_{s_comb}|)$ showed a decreasing trend to convergence with increasing u^*
 479 (Fig. 12). On average, the $|F_{s_comb}|/(|F_c|+|F_{s_comb}|)$ ranged from 17.2% to 82.0%, with a
 480 higher value during the dormant season compared to the growing season. This indicated
 481 that as turbulence intensity increased, the contribution of F_s to the NEE in forests
 482 decreased to a constant value. Nevertheless, even under strong turbulence intensity, F_s
 483 still played a significant role in the NEE observations of forests in complex terrains.



484
 485 Fig. 12 Relative contribution ratio of the CO₂ storage flux magnitude ($|F_{s_comb}|/(|F_c|+|F_{s_comb}|)$)
 486 determined by decision-level fusion model as a function of the friction velocity (u^*) moving block
 487 averages from all 30-min data for the years 2020–2021. GD represents the growing season's
 488 daytime; GN represents the growing season's nighttime; GT represents the growing season's
 489 transition period; DD represents the dormant season's daytime; DN represents the dormant
 490 season's nighttime; DT represents the dormant season's transition period.

491 As indicated in Table 3, both P_m and TCI exhibited a significant positive

492 correlation with $|F_{s_comb}|/(|F_c|+|F_{s_comb}|)$ ($P < 0.05$), while both A_m and u^* showed a
493 significant negative correlation with $|F_{s_comb}|/(|F_c|+|F_{s_comb}|)$ ($P < 0.05$). Notably,
494 seasonal variations in correlation coefficients were observed. The correlation between
495 the u^* and $|F_{s_comb}|/(|F_c|+|F_{s_comb}|)$ was more pronounced during both the dormant
496 season's transition period and the growing season, and it decreased with increasing TCI
497 values during the dormant season's daytime and nighttime.

498 Table 3 Linear regression coefficients of the relative contribution ratio of F_{s_comb}
499 magnitudes to NEE observations ($|F_{s_comb}|/(|F_c|+|F_{s_comb}|)$) —driving factors
500 relationships for the six time periods.

Time period	β_0	$\ln(P_m)^7$	$\ln(A_m)^8$	$u^*{}^9$	TCI ¹⁰	$u^*:TCI$	R^2
Total	0.292 ***	0.048 ***	-0.037 ***	-0.334 ***	0.790 ***	-1.018 ***	0.278 ***
GD ¹	0.299 ***	0.016	-0.041 ***	-0.183 ***	-0.293 *	0.239	0.158 ***
GN ²	0.370 ***	0.029	-0.023 ***	-0.386 ***	-0.038	0.081	0.103 ***
GT ³	0.161	0.060 ***	-0.014 ***	-0.182	1.056 ***	-1.754	0.186 ***
DD ⁴	0.393 ***	0.011	-0.020 ***	-0.154 *	0.306	-0.153	0.040 ***
DN ⁵	0.661 ***	0.012	-0.026 ***	-0.443 ***	-0.035	0.399	0.088 ***
DT ⁶	0.495 ***	0.017	-0.036 ***	-0.294 ***	0.564	-0.852	0.149 ***

501 ¹ GD represents the growing season's daytime; ² GN represents the growing season's nighttime;
502 ³ GT represents the growing season's transition period; ⁴ DD represents the dormant season's
503 daytime; ⁵ DN represents the dormant season's nighttime; ⁶ DT represents the dormant season's
504 transition period. ⁷ A_m : maximum amplitude; ⁸ P_m : corresponding period of maximum amplitude. ⁹
505 u^* : friction velocity; ¹⁰ TCI: terrain complexity index; *** represents $P < 0.001$; ** represents $P <$
506 0.01; and * represents $P < 0.05$.

507 To evaluate the impact of F_{s_comb} on NEE_{obs} ($F_c + F_s$), we further evaluated the
508 slope (with intercept terms forced to zero) and NRMSE of $F_c + F_{s_comb}$ compared to F_c
509 + F_{s_28} , as presented in Supplementary Materials Table 7 and Table 8. The F_{s_28} in the
510 three forest stands was underestimated by 28.6%–33.3% compared to the F_{s_comb} , and
511 the NRMSE of F_{s_comb} versus the F_{s_28} ranged from 59.2% to 67.2%. The NEE_{obs} with
512 F_{s_28} was underestimated by 1.9%–4.3% compared to the NEE_{obs} with F_{s_comb} . The
513 NRMSE of NEE_{obs} with the F_{s_comb} versus the F_{s_28} in the three forest stands ranged
514 from 16.0% to 25.4%. The analysis suggested that combining the F_s values based on
515 different averaging [CO₂] time windows in the decision-level fusion model could
516 successfully weigh potential underestimation bias and random uncertainties.

517 The influences of F_s on the relationship between NEE observations and
518 meteorological drivers, indicated the effect of uncertainty in F_s estimates on NEE
519 observations. Our analysis showed that the correlations between NEE observations
520 derived from $F_c + F_s$ and both photosynthetic photon flux density (PPFD) and air
521 temperature are lower compared to those obtained from F_c alone (Figure 1 and Figure
522 2 in the Supplementary Materials). Additionally, the estimated light saturated net CO₂
523 assimilation (A_{max}) is greater when NEE observations are estimated by $F_s + F_c$, as
524 opposed to when NEE is estimated solely by F_c . This suggests that F_s significantly
525 affects daytime NEE and can correct the estimation of A_{max} and related parameters. The
526 relationship between NEE observations and PPFD is influenced by the size of averaging
527 time window the F_s measurement. A larger averaging window results in less random
528 uncertainty in the F_s estimation, thereby increasing the correlation between NEE

529 observations and meteorological drivers, including PPFD and T_a .

530 **4 Discussion**

531 4.1 Short-term $[CO_2]$ fluctuations above the forest canopy and F_s estimates in complex 532 terrains

533 Compared to flat and uniform underlying surface, complex terrain and
534 heterogeneous canopies modify the trajectory, speed distribution, and direction of the
535 airflow. Increased wind speeds and shifting wind directions also increase turbulent
536 activity above the canopy, facilitating the mixing and dispersion of CO_2 . This study
537 found that short-term fluctuations of $[CO_2]$ above the canopy exhibited a range of 1 to
538 10 min (Fig. 2). These fluctuations were characterized by an average P_m ranging from
539 2.313 to 2.784 min (Table 2). Our results are in line with previous research using
540 wavelet analysis, which reported fluctuation periods of $[CO_2]$ within and above the
541 forest canopy to be between 14 and 116 s (Cava et al., 2004). Their observations of the
542 canopy waves during periods of extreme atmospheric stability (when $z/L \gg 1$) exhibited
543 a dominant period of 1–2 min, consistent with our findings. The period of $[CO_2]$
544 fluctuations was found to be predominantly influenced by turbulent fluxes and the
545 residence time of CO_2 within the canopy. This indicated a potential correlation between
546 P_m and the residence time of CO_2 within the canopy. Fuentes et al. (2006) employed a
547 Lagrangian model and calculated the residence time of air parcels released near the
548 ground and canopy, finding values ranging from 3 to 10 min and from 1 to 10 min,
549 respectively. Similarly, Edburg et al. (2011) used the standard deviation of $[CO_2]$

550 averages to determine CO₂ residence time at different locations, including the ground,
551 within the canopy, and in their gas mixtures, yielding values of 8.6, 3.6, and 5.6 min,
552 respectively. The results of these simulation experiments are consistent with our study,
553 further supporting the association between [CO₂] fluctuations above the forest canopy
554 and CO₂ residence time.

555 Tree density and canopy structure also play a role in influencing the air parcel
556 residence time; in flat terrains, the air parcel residence time correlate with u^* (Gerken
557 et al., 2017), and an increase in vegetation leaf area leads to longer residence times
558 when turbulence is not fully penetrative. During the growing season, forests in our study
559 site exhibit higher leaf area index and greater canopy densities than during the dormant
560 season (Li et al., 2023), resulting in longer P_m of short-term [CO₂] fluctuations above
561 the canopy (Fig. 3). Additionally, at night, stable atmospheric conditions lead to longer
562 residence times due to suppressed turbulent mixing, resulting in relatively long
563 nighttime P_m values compared to daytime and transition periods (Fig. 3).

564 Complex terrains introduce complex changes in air flow structures, including
565 gravity-induced waves, drainage, and nonlinear waves induced by single gusts, leading
566 to dramatic [CO₂] fluctuations. These dynamics contribute to uncertainties in estimating
567 F_s . During night, the difference between incoming and outgoing longwave radiation
568 over the valley soil surface and vegetation canopy gives rise to radiative cooling.
569 Subsequently, the air near the soil surface experiences a gravity-induced downslope
570 acceleration, potentially causing katabatic flow. As inertia-driven upslope winds are
571 halted by katabatic acceleration, a local shallow drainage flow is established, reaching

572 a quasi-equilibrium state approximately 1.5 h after sunset (Nadeau et al., 2013). Under
573 stable atmospheric conditions, even gentle slopes (around 1°) can generate strong
574 gravity-driven waves (Belušić and Mahrt, 2012). Consequently, advection may
575 complicate the interpretation of nighttime EC measurements at certain relatively gentle
576 sites, but this complexity is not evident during daytime measurements (Leuning et al.,
577 2008). Advection plays a role in depleting the CO₂ accumulated within the canopy,
578 resulting in lower F_s fluxes and establishing an inverse relationship between storage
579 and advection (Van Gorsel et al., 2011). The occurrence of larger F_s values for long P_m
580 values suggests weaker advection compared to short P_m values (Fig. 4). In our study,
581 we observed that the F_s magnitude was relatively large during nighttime and transition
582 periods, while it was smaller during daytime (Fig. 4), which is consistent with the
583 findings reported by Wang et al. (2016).

584 The terrain unevenness and the complexity of canopy structure significantly affect
585 the airflow divergence in the atmospheric boundary layer. This results in weakened air
586 circulation within the canopy and spatial variation in the patterns and extent of airflow
587 separation (Grant et al., 2015). During nighttime and transition periods in a closed
588 canopy, the turbulent coupling state above and below the canopy gradually decouples,
589 eventually reaching complete decoupling as the u^* decreases (Fig. 5). However, this
590 decoupling does not lead to stable stratification within the canopy. Despite the
591 occurrence of decoupling and advection in the closed canopy, waves are unlikely to
592 exist within the canopy itself (Van Gorsel et al., 2011). As a result, a consistent trend
593 in the variation of F_s with τ is observed across the three forest stands during the growing

594 season, independent of P_m (Fig. 9). Conversely, in an open canopy where waves are
595 present, the observations of F_s become more complex. This complexity could be the
596 primary reason why the variation of F_s with $[CO_2]$ averaging time windows differs
597 between the three forest stands for short P_m values during the dormant season daytime
598 (Fig. 9). The presence of waves introduces additional variability in the measurements,
599 leading to differences in F_s estimates based on different $[CO_2]$ averaging time windows
600 in these particular conditions.

601 4.2 Uncertainty in forest ecosystem F_s measurement in complex terrains

602 The random uncertainty of F_s shares similarities with NEE estimation. For
603 example, the magnitude of F_s measurements is positively correlated with the standard
604 deviation of random uncertainty in F_s . Additionally, the overall distribution of F_s
605 measurements exhibits a non-Gaussian distribution with a high peak, aligning with the
606 statistical properties of NEE uncertainty (Richardson et al., 2006; Richardson et al.,
607 2008). The uncertainty in the storage term depends a lot on the set-up used, together
608 with the biological activity of the ecosystem, and the height of the control volume. In
609 addition, various factors contribute to the uncertainty in F_s estimates, including flux
610 measurement footprint variations, sampling frequency, spatial sampling resolution of
611 CO_2/H_2O concentrations, and instrumental measurement accuracy. The accuracy and
612 precision requested for the CO_2 and H_2O concentration measurements are $\pm 1 \mu mol$
613 mol^{-1} and $\pm 1 mmol mol^{-1}$, respectively (Montagnani et al., 2018). The uncertainty
614 arising from variations in the flux measurement footprint is considerable, typically on
615 the order of tens of percentages, which is an order of magnitude higher than typical

616 sensor errors (Metzger, 2018). The AP200 adopts buffer volumes to mix the gas. The
617 LI-850 analyzer integrated within in AP200 exhibits a sensitivity to water vapor of less
618 than $0.1 \mu\text{mol CO}_2$ per $\text{mmol mol}^{-1} \text{H}_2\text{O}$, and a sensitivity to CO_2 of less than 0.0001
619 $\text{mmol mol}^{-1} \text{H}_2\text{O}$ per $\mu\text{mol CO}_2$. Efforts to reduce random errors in $[\text{CO}_2]$ originating
620 from pressure fluctuations include adding buffer volumes before IRGA pumping tests
621 (Marcolla et al., 2014). The buffer volumes are fully mixed during gas extraction and
622 performs a weighted average of $[\text{CO}_2]$ instantaneous measurements to minimize the
623 sampling error for each level's $[\text{CO}_2]$ measurement (Cescatti et al., 2016).

624 The F_s estimates can be influenced by singular eddies that penetrate inside the
625 canopy (Finnigan, 2006). Accurate calculation of F_s requires considering the period of
626 $[\text{CO}_2]$ fluctuations with the eddy coherence structure. The spectral energy of the F_s time
627 series is primarily concentrated between 0.001 and 0.2 Hz (500 and 5 s , respectively).
628 However, even with sampling frequencies of 2 Hz and below, significantly lower F_s
629 values are obtained (Bjorkegren et al., 2015). The Nyquist-Shannon sampling theorem
630 dictates that accurate measurements of $[\text{CO}_2]$ require a sampling period no longer than
631 half the period of $[\text{CO}_2]$ fluctuations. Consequently, to monitor short-term changes in
632 $[\text{CO}_2]$, measurements must be taken over a period no longer than half of the period
633 corresponding to the maximum amplitude (or major energy) of $[\text{CO}_2]$ fluctuations. In
634 this study, the average P_m for $[\text{CO}_2]$ fluctuations fell within the range of 2.313 – 2.784
635 min (Table 2). Therefore, it is crucial to ensure that the sampling period for $[\text{CO}_2]$ does
636 not exceed 1.256 to 1.392 min, which corresponds to half the average P_m range.
637 Monitoring fluctuations of P_m for less than 4 min during a 2 -min monitoring period of

638 [CO₂] presents a significant challenge. This is a primary reason that the systematic bias
639 and random error in F_s estimate with a single profile system are irreconcilable (Wang
640 et al., 2016). Short-term [CO₂] fluctuations are mainly influenced by boundary layer
641 turbulence, and sampling errors in incomplete fluctuation cycles will be superimposed
642 with the real advection flux (anisotropy) dispersion in complex terrains (Van Gorsel et
643 al., 2011). This substantially increases the random uncertainty in F_s based on shorter
644 [CO₂] averaging time windows (Fig. 6 and Fig. 8). As a result, the deviation of NEE
645 estimates from the actual value expands.

646 Fluxes in heterogeneous regions are significantly higher than in uniform regions.
647 The energy transfer from the ground surface to large eddies occurs primarily in areas
648 with pronounced heterogeneity, and this energy distribution is uneven across the region
649 (Aubinet et al., 2012). Once large-scale eddies acquire energy, their cascading of energy
650 to smaller-scale eddies is influenced by topographic features, leading to variations in
651 these smaller-scale eddies along different flow streams (Chen et al., 2023). In complex
652 terrains, the bidirectional airflow within forests along slopes can cause the decoupling
653 of soil CO₂ fluxes from EC measurements above the forest canopy (Feigenwinter et al.,
654 2008; Aubinet et al., 2003), leading to significant errors in CO₂ flux measurements.
655 Forest soil serves as the primary source of CO₂ gas and regions of high flux over
656 complex terrains act like chimneys, transporting air parcels from the soil surface within
657 forests (Chen et al., 2019). By increasing the number of gas concentration sampling
658 points near the ground, the horizontal representativeness can be enhanced, thereby
659 reducing the bias in the estimation of F_s (Nicolini et al., 2018). In situations where

660 turbulence is not well-developed, and CO₂ mixing is inadequate, the trend of F_s with
661 turbulence intensity aligns with that of advective fluxes, which is opposite to that of
662 turbulent fluxes (Mchugh et al., 2017). The temporal dynamics and amplitudes of F_s
663 changes are influenced by topography complexity and wind conditions above the forest
664 canopy (Fig. 10). Locations with more complex and sloping topography at the flux
665 tower are more likely to generate advective fluxes that may not be easily observed at a
666 single point.

667 Estimating landscape CO₂ fluxes in complex terrains solely based on
668 measurements from a single flux tower can introduce significant errors and biases that
669 are not acceptable. The magnitude of these errors in F_s estimates is dependent on the
670 height of the forest canopy and the endogenous source/sink (Chen et al., 2020). To
671 mitigate errors and biases associated with estimating F_s in complex terrains, we
672 employed a regression modeling approach using the decision-level fusion model. This
673 method involves computing a weighted average of F_s based on different [CO₂]
674 averaging time windows, effectively reducing errors and biases in the estimation of F_s
675 (see Table 5). In fact, from the definition of storage flux, it can be seen that weighting
676 the storage flux is essentially weighting the [CO₂] in the average time window, which
677 means replacing spatial sequences with temporal sequences for weighting. The
678 weighting coefficients used to construct the model were based on the relative errors and
679 biases of F_s estimation, with the weighting coefficient decreasing as the represented
680 moment's length increased. To obtain more accurate estimates of forest ecosystem F_s in
681 complex terrains, further research should focus on understanding the spatiotemporal

682 patterns and dynamics of [CO₂].

683 **5 Conclusions**

684 This study investigated the impact of short-term [CO₂] fluctuations on the
685 estimation of F_s in temperate forest ecosystems within complex terrains. Additionally,
686 it examined the F_s uncertainty and the contribution of the F_s to NEE using data from
687 three flux towers. To enhance F_s uncertainty estimation, statistical sampling techniques
688 were applied based on the individual tower approach.

689 The results highlighted the significance of considering multiple time windows for
690 averaging [CO₂] when estimating F_s, as [CO₂] above the forest canopies exhibited
691 fluctuations with periods ranging from 1 to 10 minutes. Diurnal, seasonal, and spatial
692 variations were observed in the amplitude and periodicity of [CO₂] fluctuations,
693 highlighting the need for thoughtful sampling strategies. The use of individual gas
694 analyzers to sample the CO₂ in the control volume was inadequate, leading to
695 systematic biases and random errors in the F_s estimates. Increasing [CO₂] averaging
696 time windows mitigated the effect of [CO₂] fluctuations on F_s estimates, reducing both
697 their magnitude and uncertainty.

698 The study also revealed that the uncertainty of F_s followed a non-normal
699 distribution, with its standard deviation positively correlated with F_s magnitude, which
700 has important implications for quality control. To improve F_s estimation, a decision-
701 level fusion model was introduced, integrating F_s estimates from multiple [CO₂]
702 averaging time windows, effectively reducing the impact of short-term [CO₂]

703 fluctuations while considering underestimation bias and random errors. The
704 contribution of F_s to NEE exhibited diurnal, seasonal, and spatial variations associated
705 with u^* , contributing to the NEE observations at rates ranging from 17.2% to 82.0%
706 depending on the turbulent mixing and terrain complexity. The influence of terrain
707 complexity on the relationship between $[CO_2]$ fluctuations, turbulent mixing, and the
708 contribution of F_s to NEE was also evident. The findings from the three flux towers
709 allowed for the generalization of these results beyond the study site. These insights
710 provide crucial scientific support for the practical application of the eddy covariance
711 technique and advance our understanding of accurately estimating NEE in forest
712 ecosystems in complex terrains.

713 **Appendix A**

714 *A.1 the weight parameters of the decision-level fusion model*

715 For each 30-min CO_2 storage flux (F_s) estimate based on the CO_2 concentration
716 ($[CO_2]$) averaging time window (τ), the weight in the decision-level fusion model can
717 be obtained by weighting the random uncertainty and bias of F_{s_τ} .

718 The weight of the random uncertainty for the F_{s_τ} is expressed as follows:

$$w_\tau = \frac{1/\sigma(\varepsilon_\tau)}{\sum_j 1/\sigma(\varepsilon_j)}, \quad (A.1)$$

719 where $\sigma(\varepsilon_\tau)$ is the random uncertainty of the F_{s_τ} , qualified as the standard deviation.

720 The weight of the bias for the F_{s_τ} is expressed as follows:

$$W_\tau = \frac{K_\tau}{\sum_j K_j}, \quad (A.2)$$

721 where K_τ is the slope between the F_{s_τ} and $F_{s_{28}}$.

722 Ultimately, the weight of the F_{s_τ} in the decision-level fusion model can be

723 calculated using the following equation:

$$w_{\tau}^* = rw_{\tau} + (1 - r)W_{\tau}, \quad (\text{A.3})$$

724 where r represents the proportion of the weight of random uncertainty.

725 A.2 Complex terrain index

726 This study employed a novel descriptor called the terrain complexity index (*TCI*)
727 to quantify the complexity of the three-dimensional terrain. For a given unit area, the
728 *TCI* equation can be expressed as follows:

$$TCI = (1 - P_d \cos \alpha_d)(1 - Z_d^{-1})(D_f - 2)^{-H/\ln(12)}, \quad (\text{A.4})$$

729 where, P_d represents the volume of terrain above the lowest elevation of an area
730 unit (V_u) divided by the product of its largest vertically projected area (S_v) and the
731 edge length of the side of the area unit (d), expressed as $P_d = V_u/(S_v d)$; P_d was
732 defined to be one when the S_v is zero. Given V_u , an increase in S_v correlates with a
733 higher degree of terrain complexity. Notably, the P_d is defined as 1 when the terrain
734 volume is 0 or when the terrain surface of the area unit was parallel to the horizontal
735 plane and was smooth and homogeneous. α_d indicates the slope of the area unit. Z_d
736 denoted the terrain roughness, which defined as the ratio of the terrain surface area to
737 the projected horizontal plane (Loke and Chisholm, 2022). The value of Z_d is in the
738 range of $[1, +\infty)$. The larger Z_d , the more complex the terrain. D_f is the fractal
739 dimension of terrain surface area, which ranged from 2 to 3 and described the
740 complexity in spatially self-similar structure of the local surface within the area unit
741 and the area unit surface (B. B. Mandelbrot, 1967; Taud and Parrot, 2005). Employing
742 terrain surface area, the box-counting method is used to estimate fractal dimension of

743 unit area. H represented the Shannon-Wiener index and expressed as $H =$
744 $-\sum_{i=1}^n P_i \ln(P_i)$, capturing the uniformity of the spatial distribution of the pixel
745 aspects within the area unit (Brown, 1997). When the aspect of each pixel is divided
746 into 30° segments, P_i denotes the proportion of the i^{th} type of pixel aspects within the
747 area unit and n was the total number of pixel aspect types within the area unit. A
748 larger H indicates a more complex terrain. When the number of pixel aspect types in
749 the area unit is kept constant, it's essential to recognize that greater uniformity in the
750 distribution of all pixel aspect in the area unit results in a larger H . Similarly, when the
751 uniformity of the distribution of pixel aspects in the area unit is kept constant, a larger
752 H is achieved with an increase in the observation of the number of pixel aspect types.

753 To quantify the terrain complexity of the underlying surface around the flux towers,
754 we computed the quartiles of TCI for all area units within a sector (divided by 30°) with
755 a radius of 380 m. A weighted geometric mean was employed to construct $TCIs$, which
756 describe the statistical distribution of TCI of the sector. The $TCIs$ represents the
757 topographic complexity of the sector and are calculated using the following equation:

$$758 \quad TCI_s = (TCI_5 TCI_{25} TCI_{50} TCI_{75} TCI_{95})^{1/5} \quad (\text{A.5})$$

759 where TCI_5 , TCI_{25} , TCI_{50} , TCI_{75} , and TCI_{95} are the quartiles of 5%, 25%, 50%, 75%,
760 and 95%, respectively. The $TCIs$ values range from 0 to 1, with higher values indicating
761 greater terrain complexity.

762 *Data availability.* Data used in this paper are available at the Science Data Bank
763 (<https://www.scidb.cn/en/s/7ZfQZv>) or upon request to the corresponding author.

764 *Author contributions.* DT developed the manuscript; JZ was responsible for

765 conceptualizing the idea and designing the research study; TG substantially structured
766 the manuscript; FY contributed to the data collection process; YZ helped in the design
767 and preparation of the figures and tables; XZ and BY revised the manuscript.

768 *Competing interests.* The authors declare that they have no known competing
769 financial interests or personal relationships that could have appeared to influence the
770 work reported in this paper.

771 *Acknowledgments.* We are grateful to Qingyuan Forest CERN, Chinese Academy of
772 Sciences/Qingyuan Forest, National Observation and Research Station, Liaoning
773 Province, China for providing forest sites, instrument systems, and logistic supports.

774 *Financial support.* This research was financially supported by the National Natural
775 Science Foundation of China (No. 32192435), the China Postdoctoral Science
776 Foundation (No. 2023M733672), Key R&D Program of Liaoning Province
777 (2023JH2/101800043), and the Postdoctoral Research Startup Foundation of Liaoning
778 Province of China (No. 2022-BS-022).

779 **Reference**

780 Aubinet, M., Heinesch, B., and Yernaux, M.: Horizontal and Vertical CO₂ Advection In A Sloping Forest,
781 *Boundary-Layer Meteorology*, 108, 397-417, 10.1023/a:1024168428135, 2003.

782 Aubinet, M., Vesala, T., and Papale, D.: *Eddy Covariance: A Practical Guide to Measurement and Data*
783 *Analysis*, Springer Atmospheric Sciences, Springer, Dordrecht, XXII, 438 pp., 10.1007/978-94-007-
784 2351-1, 2012.

785 Aubinet, M., Grelle, A., Ibrom, A., Rannik, Ü., Moncrieff, J., Foken, T., Kowalski, A. S., Martin, P. H.,
786 Berbigier, P., Bernhofer, C., Clement, R., Elbers, J., Granier, A., Grünwald, T., Morgenstern, K.,
787 Pilegaard, K., Rebmann, C., Snijders, W., Valentini, R., and Vesala, T.: Estimates of the Annual Net
788 Carbon and Water Exchange of Forests: The EUROFLUX Methodology, in: *Advances in Ecological*
789 *Research Volume 30, Advances in Ecological Research*, 113-175, 10.1016/s0065-2504(08)60018-5,
790 2000.

791 B. B. Mandelbrot: How Long Is the Coast of Britain? Statistical Self-Similarity and Fractional Dimension,
792 *Science*, 156, 636-638, 1967.

793 Belušić, D. and Mahrt, L.: Is geometry more universal than physics in atmospheric boundary layer flow?,

794 Journal of Geophysical Research: Atmospheres, 117, n/a-n/a, 10.1029/2011jd016987, 2012.

795 Bjorkegren, A. B., Grimmond, C. S. B., Kotthaus, S., and Malamud, B. D.: CO₂ emission estimation in
796 the urban environment: Measurement of the CO₂ storage term, Atmospheric Environment, 122, 775-790,
797 10.1016/j.atmosenv.2015.10.012, 2015.

798 Brown, S.: Estimating Biomass and Biomass Change of Tropical Forests: A Primer, FAO Forestry Paper,
799 134, 1997.

800 Cava, D., Giostra, U., Siqueira, M., and Katul, G.: Organised motion and radiative perturbations in the
801 nocturnal canopy sublayer above an even-aged pine forest, Boundary-Layer Meteorology, 112, 129-157,
802 DOI 10.1023/B:BOUN.0000020160.28184.a0, 2004.

803 Cescatti, A., Marcolla, B., Goded, I., and Gruening, C.: Optimal use of buffer volumes for the
804 measurement of atmospheric gas concentration in multi-point systems, Atmospheric Measurement
805 Techniques, 9, 4665-4672, 10.5194/amt-9-4665-2016, 2016.

806 Chen, B., Chamecki, M., and Katul, G. G.: Effects of topography on in-canopy transport of gases emitted
807 within dense forests, Quarterly Journal of the Royal Meteorological Society, 145, 2101-2114,
808 10.1002/qj.3546, 2019.

809 Chen, B. C., Chamecki, M., and Katul, G. G.: Effects of Gentle Topography on Forest-Atmosphere Gas
810 Exchanges and Implications for Eddy-Covariance Measurements, J Geophys Res-Atmos, 125, ARTN
811 e2020JD032581
812 10.1029/2020JD032581, 2020.

813 Chen, J., Chen, X., Jia, W., Yu, Y., and Zhao, S.: Multi-sites observation of large-scale eddy in surface
814 layer of Loess Plateau, Science China Earth Sciences, 66, 871–881, [https://doi.org/10.1007/s11430-022-](https://doi.org/10.1007/s11430-022-1035-4)
815 [1035-4](https://doi.org/10.1007/s11430-022-1035-4), 2023.

816 de Araújo, A. C., J.P.H.B., O., Dolman, A. J., B., K., M.J., W., and J.R., E.: Implications of CO₂ pooling
817 on delta C13 of ecosystem respiration and leaves in Amazonian forest, Biogeosciences, 5, 779-795,
818 10.5194/bg-5-779-2008, 2008.

819 de Araújo, A. C., Dolman, A. J., Waterloo, M. J., Gash, J. H. C., Kruijt, B., Zanchi, F. B., de Lange, J. M.
820 E., Stoevelaar, R., Manzi, A. O., Nobre, A. D., Lootens, R. N., and Backer, J.: The spatial variability of
821 CO₂ storage and the interpretation of eddy covariance fluxes in central Amazonia, Agricultural and Forest
822 Meteorology, 150, 226-237, 10.1016/j.agrformet.2009.11.005, 2010.

823 Edburg, S. L., Stock, D., Lamb, B. K., and Patton, E. G.: The Effect of the Vertical Source Distribution
824 on Scalar Statistics within and above a Forest Canopy, Boundary-Layer Meteorology, 142, 365-382,
825 10.1007/s10546-011-9686-1, 2011.

826 Feigenwinter, C., Bernhofer, C., and Vogt, R.: The Influence of Advection on the Short Term CO₂-Budget
827 in and Above a Forest Canopy, Boundary-Layer Meteorology, 113, 201-224,
828 10.1023/B:BOUN.0000039372.86053.ff, 2004.

829 Feigenwinter, C., Bernhofer, C., Eichelmann, U., Heinesch, B., Hertel, M., Janous, D., Kolle, O.,
830 Lagergren, F., Lindroth, A., Minerbi, S., Moderow, U., Mölder, M., Montagnani, L., Queck, R., Rebmann,
831 C., Vestin, P., Yernaux, M., Zeri, M., Ziegler, W., and Aubinet, M.: Comparison of horizontal and vertical
832 advective CO₂ fluxes at three forest sites, Agricultural and Forest Meteorology, 148, 12-24,
833 10.1016/j.agrformet.2007.08.013, 2008.

834 Finnigan, J.: The storage term in eddy flux calculations, Agricultural and Forest Meteorology, 136, 108-
835 113, 10.1016/j.agrformet.2004.12.010, 2006.

836 Finnigan, J., Ayotte, K., Harman, I., Katul, G., Oldroyd, H., Patton, E., Poggi, D., Ross, A., and Taylor,
837 P.: Boundary-Layer Flow Over Complex Topography, Boundary-Layer Meteorology, 177, 247-313,

838 10.1007/s10546-020-00564-3, 2020.

839 Fuentes, J. D., Wang, D., Bowling, D. R., Potosnak, M., Monson, R. K., Goliff, W. S., and Stockwell, W.
840 R.: Biogenic Hydrocarbon Chemistry within and Above a Mixed Deciduous Forest, *Journal of*
841 *Atmospheric Chemistry*, 56, 165-185, 10.1007/s10874-006-9048-4, 2006.

842 Gao, T., Yu, L.-Z., Yu, F.-Y., Wang, X.-C., Yang, K., Lu, D.-L., Li, X.-F., Yan, Q.-L., Sun, Y.-R., Liu, L.-
843 F., Xu, S., Zhen, X.-J., Ni, Z.-D., Zhang, J.-X., Wang, G.-F., Wei, X.-H., Zhou, X.-H., and Zhu, J.-J.:
844 Functions and applications of Multi-Tower Platform of Qingyuan Forest Ecosystem Research Station of
845 Chinese Academy of Sciences, *Chinese journal of applied ecology*, 31, 695-705, 10.13287/j.1001-
846 9332.202003.040, 2020.

847 Gerken, T., Chamecki, M., and Fuentes, J. D.: Air-Parcel Residence Times Within Forest Canopies,
848 *Boundary-Layer Meteorology*, 165, 29-54, 10.1007/s10546-017-0269-7, 2017.

849 Grant, E. R., Ross, A. N., Gardiner, B. A., and Mobbs, S. D.: Field Observations of Canopy Flows over
850 Complex Terrain, *Boundary-Layer Meteorology*, 156, 231-251, 10.1007/s10546-015-0015-y, 2015.

851 Gu, L., Massman, W. J., Leuning, R., Pallardy, S. G., Meyers, T., Hanson, P. J., Riggs, J. S., Hosman, K.
852 P., and Yang, B.: The fundamental equation of eddy covariance and its application in flux measurements,
853 *Agricultural and Forest Meteorology*, 152, 135-148, 10.1016/j.agrformet.2011.09.014, 2012.

854 Heinesch, B., Yernaux, M., and Aubinet, M.: Some methodological questions concerning advection
855 measurements: a case study, *Boundary-Layer Meteorology*, 122, 457-478, 10.1007/s10546-006-9102-4,
856 2007.

857 Hollinger, D. Y. and Richardson, A. D.: Uncertainty in eddy covariance measurements and its application
858 to physiological models, *Tree Physiol*, 25, 873-885, DOI 10.1093/treephys/25.7.873, 2005.

859 Huang, N. E. and Wu, Z.: A review on Hilbert-Huang transform: Method and its applications to
860 geophysical studies, *Reviews of Geophysics*, 46, 10.1029/2007rg000228, 2008.

861 Huang, N. E., Shen, Z., Long, S. R., Wu, M. C., Shih, H. H., Zheng, Q., Yen, N.-C., Tung, C. C., and Liu,
862 H. H.: The empirical mode decomposition and the Hilbert spectrum for nonlinear and non-stationary
863 time series analysis, *Proceedings of the Royal Society of London. Series A: Mathematical, Physical and*
864 *Engineering Sciences*, 454, 903-995, 10.1098/rspa.1998.0193, 1998.

865 Khélifa, N., Lecollinet, M., and Himbert, M.: Molar mass of dry air in mass metrology, *Measurement*,
866 40, 779-784, 10.1016/j.measurement.2006.05.009, 2007.

867 Leuning, R., Zegelin, S. J., Jones, K., Keith, H., and Hughes, D.: Measurement of horizontal and vertical
868 advection of CO₂ within a forest canopy, *Agricultural and Forest Meteorology*, 148, 1777-1797,
869 10.1016/j.agrformet.2008.06.006, 2008.

870 Li, S., Yan, Q., Liu, Z., Wang, X., Yu, F., Teng, D., Sun, Y., Lu, D., Zhang, J., Gao, T., and Zhu, J.:
871 Seasonality of albedo and fraction of absorbed photosynthetically active radiation in the temperate
872 secondary forest ecosystem: A comprehensive observation using Qingyuan Ker towers, *Agricultural and*
873 *Forest Meteorology*, 333, 10.1016/j.agrformet.2023.109418, 2023.

874 Li, Y.-C., Liu, F., Wang, C.-K., Gao, T., and Wang, X.-C.: Carbon budget estimation based on different
875 methods of CO₂ storage flux in forest ecosystems, *Chinese journal of applied ecology*, 31, 3665-3673,
876 10.13287/j.1001-9332.202011.004, 2020.

877 Loke, L. H. L. and Chisholm, R. A.: Measuring habitat complexity and spatial heterogeneity in ecology,
878 *Ecology Letters*, 25, 2269-2288, 10.1111/ele.14084, 2022.

879 Marcolla, B., Cobbe, I., Minerbi, S., Montagnani, L., and Cescatti, A.: Methods and uncertainties in the
880 experimental assessment of horizontal advection, *Agricultural and Forest Meteorology*, 198-199, 62-71,
881 10.1016/j.agrformet.2014.08.002, 2014.

882 McHugh, I. D., Beringer, J., Cunningham, S. C., Baker, P. J., Cavagnaro, T. R., Mac Nally, R., and
883 Thompson, R. M.: Interactions between nocturnal turbulent flux, storage and advection at an "ideal"
884 eucalypt woodland site, *Biogeosciences*, 14, 3027-3050, 10.5194/bg-14-3027-2017, 2017.

885 McMaster, G. S. and Wilhelm, W. W.: Growing degree-days: one equation, two interpretations,
886 *Agricultural and Forest Meteorology*, 87, 291-300, Doi 10.1016/S0168-1923(97)00027-0, 1997.

887 Metzger, S.: Surface-atmosphere exchange in a box: Making the control volume a suitable representation
888 for in-situ observations, *Agricultural and Forest Meteorology*, 255, 68-80,
889 10.1016/j.agrformet.2017.08.037, 2018.

890 Montagnani, L., Grunwald, T., Kowalski, A., Mammarella, I., Merbold, L., Metzger, S., Sedlak, P., and
891 Siebicke, L.: Estimating the storage term in eddy covariance measurements: the ICOS methodology, *Int*
892 *Agrophys*, 32, 551-567, 10.1515/intag-2017-0037, 2018.

893 Montagnani, L., Manca, G., Canepa, E., Georgieva, E., Acosta, M., Feigenwinter, C., Janous, D.,
894 Kerschbaumer, G., Lindroth, A., Minach, L., Minerbi, S., Mölder, M., Pavelka, M., Seufert, G., Zeri, M.,
895 and Ziegler, W.: A new mass conservation approach to the study of CO₂ advection in an alpine forest,
896 *Journal of Geophysical Research*, 114, 10.1029/2008jd010650, 2009.

897 Nadeau, D. F., Pardyjak, E. R., Higgins, C. W., Huwald, H., and Parlange, M. B.: Flow during the evening
898 transition over steep Alpine slopes, *Quarterly Journal of the Royal Meteorological Society*, 139, 607-624,
899 10.1002/qj.1985, 2013.

900 Nicolini, G., Aubinet, M., Feigenwinter, C., Heinesch, B., Lindroth, A., Mamadou, O., Moderow, U.,
901 Mölder, M., Montagnani, L., Rebmann, C., and Papale, D.: Impact of CO₂ storage flux sampling
902 uncertainty on net ecosystem exchange measured by eddy covariance, *Agricultural and Forest*
903 *Meteorology*, 248, 228-239, 10.1016/j.agrformet.2017.09.025, 2018.

904 Richardson, A. D., Hollinger, D. Y., Burba, G. G., Davis, K. J., Flanagan, L. B., Katul, G. G., William
905 Munger, J., Ricciuto, D. M., Stoy, P. C., Suyker, A. E., Verma, S. B., and Wofsy, S. C.: A multi-site
906 analysis of random error in tower-based measurements of carbon and energy fluxes, *Agricultural and*
907 *Forest Meteorology*, 136, 1-18, 10.1016/j.agrformet.2006.01.007, 2006.

908 Richardson, A. D., Mahecha, M. D., Falge, E., Kattge, J., Moffat, A. M., Papale, D., Reichstein, M.,
909 Stauch, V. J., Braswell, B. H., Churkina, G., Kruijt, B., and Hollinger, D. Y.: Statistical properties of
910 random CO₂ flux measurement uncertainty inferred from model residuals, *Agricultural and Forest*
911 *Meteorology*, 148, 38-50, 10.1016/j.agrformet.2007.09.001, 2008.

912 Sha, J., Zou, J., and Sun, J.: Observational study of land-atmosphere turbulent flux exchange over
913 complex underlying surfaces in urban and suburban areas, *SCIENCE CHINA-EARTH SCIENCES*, 64,
914 1050-1064, 10.1007/s11430-020-9783-2, 2021.

915 Siebicke, L., Steinfeld, G., and Foken, T.: CO₂-gradient measurements using a parallel multi-analyzer
916 setup, *Atmospheric Measurement Techniques*, 4, 409-423, 10.5194/amt-4-409-2011, 2011.

917 Taud, H. and Parrot, J.-F.: Measurement of DEM roughness using the local fractal dimension,
918 *Géomorphologie : relief, processus, environnement*, 11, 327-338, 10.4000/geomorphologie.622, 2005.

919 van Gorsel, E., Harman, I. N., Finnigan, J. J., and Leuning, R.: Decoupling of air flow above and in plant
920 canopies and gravity waves affect micrometeorological estimates of net scalar exchange, *Agricultural*
921 *and Forest Meteorology*, 151, 927-933, 10.1016/j.agrformet.2011.02.012, 2011.

922 Wang, J., Shi, T., Yu, D., Teng, D., Ge, X., Zhang, Z., Yang, X., Wang, H., and Wu, G.: Ensemble
923 machine-learning-based framework for estimating total nitrogen concentration in water using drone-
924 borne hyperspectral imagery of emergent plants: A case study in an arid oasis, NW China, *Environmental*
925 *Pollution*, 266, 10.1016/j.envpol.2020.115412, 2020.

926 Wang, X., Wang, C., Guo, Q., and Wang, J.: Improving the CO₂ storage measurements with a single
927 profile system in a tall-dense-canopy temperate forest, *Agricultural and Forest Meteorology*, 228-229,
928 327-338, 10.1016/j.agrformet.2016.07.020, 2016.

929 Warton, D. I., Duursma, R. A., Falster, D. S., and Taskinen, S.: smatr 3- an R package for estimation and
930 inference about allometric lines, *Methods in Ecology and Evolution*, 3, 257-259, 10.1111/j.2041-
931 210X.2011.00153.x, 2012.

932 Webb, E. K., Pearman, G. I., and Leuning, R.: Correction of flux measurements for density effects due
933 to heat and water vapour transfer, *Quarterly Journal of the Royal Meteorological Society*, 106, 85-100,
934 10.1002/qj.49710644707, 1980.

935 Xu, K., Pingingtha-Durden, N., Luo, H., Durden, D., Sturtevant, C., Desai, A. R., Florian, C., and Metzger,
936 S.: The eddy-covariance storage term in air: Consistent community resources improve flux measurement
937 reliability, *Agricultural and Forest Meteorology*, 279, 10.1016/j.agrformet.2019.107734, 2019.

938 Yang, B., Hanson, P. J., Riggs, J. S., Pallardy, S. G., Heuer, M., Hosman, K. P., Meyers, T. P., Wullschleger,
939 S. D., and Gu, L.-H.: Biases of CO₂ storage in eddy flux measurements in a forest pertinent to vertical
940 configurations of a profile system and CO₂ density averaging, *Journal of Geophysical Research*, 112,
941 10.1029/2006jd008243, 2007.

942 Yang, P. C., Black, T. A., Neumann, H. H., Novak, M. D., and Blanken, P. D.: Spatial and temporal
943 variability of CO₂ concentration and flux in a boreal aspen forest, *J Geophys Res-Atmos*, 104, 27653-
944 27661, Doi 10.1029/1999jd900295, 1999.

945 Yao, Y., Zhang, Y., Yu, G., Song, Q., Tan, Z., and Zhao, J.: Estimation of CO₂ storage flux between forest
946 and atmosphere in a tropical forest, *Journal of Beijing Forestry University*, 33, 23-29, 2011.

947 Zhang, M., Wen, X., Yu, G.-r., Zhang, L.-m., Fu, Y., Sun, X., and Han, S.-j.: Effects of CO₂ storage flux
948 on carbon budget of forest ecosystem, *Chinese journal of applied ecology*, 21, 1201-1209, 2010.

949 Zhu, J., Gao, T., Yu, L., Yu, F., Yang, K., Lu, D., Yan, Q., Sun, Y., Liu, L., Xu, S., Zhang, J., Zheng, X.,
950 Song, L., and Zhou, X.: Functions and Applications of Multi-tower Platform of Qingyuan Forest
951 Ecosystem Research Station of Chinese Academy of Sciences (Qingyuan Ker Towers), *Bulletin of the*
952 *Chinese Academy of Sciences*, 36, 351-361, 10.16418/j.issn.1000-3045.20210304002, 2021.